

9-2018

# The Effect of Ultrasonic Power in Aluminum Wire Bonding Hardness Profiles

Matthew D. McKay

Follow this and additional works at: [https://scholarcommons.scu.edu/mech\\_mstr](https://scholarcommons.scu.edu/mech_mstr)

Part of the [Mechanical Engineering Commons](#)

---

## Recommended Citation

McKay, Matthew D., "The Effect of Ultrasonic Power in Aluminum Wire Bonding Hardness Profiles" (2018). *Mechanical Engineering Master's Theses*. 35.

[https://scholarcommons.scu.edu/mech\\_mstr/35](https://scholarcommons.scu.edu/mech_mstr/35)

This Thesis is brought to you for free and open access by the Engineering Master's Theses at Scholar Commons. It has been accepted for inclusion in Mechanical Engineering Master's Theses by an authorized administrator of Scholar Commons. For more information, please contact [rscroggin@scu.edu](mailto:rscroggin@scu.edu).

**SANTA CLARA UNIVERSITY**

Department of Mechanical Engineering

I HEREBY RECOMMEND THAT THE THESIS PREPARED  
UNDER MY SUPERVISION BY

Matthew D. McKay

ENTITLED

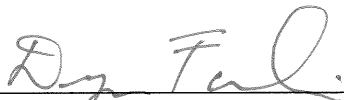
The Effect of Ultrasonic Power in Aluminum Wire Bonding  
Hardness Profiles

BE ACCEPTED IN PARTIAL FULFILLMENT OF THE REQUIREMENTS  
FOR THE DEGREE OF

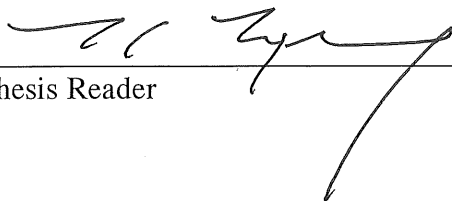
**MASTER OF SCIENCE**  
IN  
**MECHANICAL ENGINEERING**

  
\_\_\_\_\_  
Thesis Advisor

09/24/18  
\_\_\_\_\_  
date

  
\_\_\_\_\_  
Department Chair

9/28/2018  
\_\_\_\_\_  
date

  
\_\_\_\_\_  
Thesis Reader

09/27/2018  
\_\_\_\_\_  
date

# The Effect of Ultrasonic Power in Aluminum Wire Bonding Hardness Profiles

By

Matthew D. McKay

## **MASTER THESIS**

Submitted to in Partial Fulfillment of the Requirements  
For the degree of Master of Science  
In Mechanical Engineering  
In the School of Engineering at  
SANTA CLARA UNIVERSITY, September 2018

Dedicated to family and friends who supported me throughout this journey.

## **Acknowledgement**

I want to thank Dr. Sephrband for all her support and guidance on this project providing me a great learning opportunity. I would also like to thank all the great work and insight from Maddie Peuroi, Jamie Ferris and Molly Jansky. I appreciate the help and support provided by Kuliche and Soffa for the wirebonder and expertise in its use.

This work was supported by Santa Clara University, School of Engineering.

## Table of Contents

List of Tables .....	vii
List of Figures .....	viii
Abstract .....	x
1 Introduction .....	1
2 Literature Review .....	3
2.1 Types of Bonding .....	5
2.2 Bonding Parameters and Testing.....	6
2.3 Strain Hardening .....	9
2.4 Microweld Formation.....	11
2.5 Microstructure .....	12
2.6 Ultrasonic Softening.....	13
2.7 Nanoindentation .....	16
2.8 Relationship Between Hardness and Mechanical Properties .....	17
3 Methodology.....	20
3.1 Wire Bonding .....	20
3.2 Sample Preparation .....	23
3.2.1 Mounting.....	23
3.2.2 Cross Sectioning .....	23
3.2.3 Polishing .....	24
3.3 Microindentation .....	25
3.4 Optical Microscopy .....	27
3.5 Image Analysis.....	28
3.6 Nanoindentation .....	31
4 Results and Discussion .....	35
4.1 Microindentation .....	35
4.2 Wire Deformation .....	37
4.2.1 Power Dependence.....	42
4.2.2 Time Dependence .....	44
4.3 Nano-indentation.....	47
5 Conclusion.....	50
5.1 Summary and Conclusions.....	50
5.2 Future Work .....	50

6	References .....	51
	Appendix A.....	57
	Appendix B.....	58
	Appendix C.....	59
	Appendix D.....	60
	Appendix E.....	63

## **List of Tables**

Table 1-Timeline of key research into bonding mechanisms [14]. .....	4
Table 2-Key bonding parameters.....	21
Table 3-Relationship between bond tool setting and Ultrasonic Current. ....	22
Table 4-Hardness orientation data .....	36
Table 5- Bond area and calculated hardness.....	40
Table 6- Hardness in HV measured at different locations in wire and at varied bond currents. ..	42

## List of Figures

Figure 1- Ball bonding head [2]. Reproduced without permission.....	5
Figure 2- Wedge bonding [17]. Reproduced without permission.....	6
Figure 3- Pull strength vs ultrasonic power [20]. Reproduced without permission. ....	7
Figure 4- Bond pull strength vs ultrasonic power [21]. Reproduced without permission.....	8
Figure 5- Shear strength optimization for Al wire wedge bonding [23]. Reproduced without permission.....	9
Figure 6- Hardness values obtained by nanoindentation [27]. Reproduced without permission.	11
Figure 7- Grain Refinement in Al wire [35]. Reproduced without permission.....	12
Figure 8- Stress–strain compression tests with and without high-frequency vibration [28]. Reproduced without permission. ....	14
Figure 9- Microhardness of Cu balls deformed with different US [37]. Reproduced without permission.....	15
Figure 10- Correlation between microhardness and additional deformation [37]. Reproduced without permission.....	15
Figure 11- Comparison of calculated and experimental tensile strength for Al alloys [48]. Reproduced without permission. ....	18
Figure 12- Othodyne 7600HD wirebonder.....	20
Figure 13- Wires bonded to substrate.....	21
Figure 14- In Situ bonding current for different bond power settings.....	22
Figure 15- Diamond cross-sectioning saw.....	23
Figure 16- Polishing wheel.....	24
Figure 17- Microhardness tester.....	26
Figure 18- Comparison of calibrated microscope measurements to actual measurements. ....	28
Figure 19- Image analysis diagram.....	29
Figure 20- Inside of nanoindenter with sample.....	31
Figure 21- Quasi Static Trapezoid [57]. Reproduced without permission. ....	32
Figure 22- Partial Unloading profile [57]. Reproduced without permission.....	32
Figure 23- Load force vs hardness for single and multiple unloading testing.....	33
Figure 24- Orientation of Wire Cross Section.....	35
Figure 25- Schematic of bond tool and deformed wire [57]. Reproduced without permission....	37
Figure 26- Cross-section of bonded wired at varied ultrasonic currents, (a) unbonded, (b) 440 mA, (c) 880mA, (d) 1330 mA, and 1500 mA.....	38
Figure 27- (a)Wire height vs bonding current and (b) deformed cross-sectional area vs bonding current.....	39
Figure 28- Comparison of actual and theoretical hardness.....	41
Figure 29- Hardness profiles in bonded wires with different ultrasonic current.....	43
Figure 30- Schematic of Hardness profile.....	44
Figure 31- 880mA Ultrasonic Current with different hold times.....	45
Figure 32- Time dependent deformation.....	46
Figure 33- Hardness profiles from nanoindentation (a) 440 mA (b) 880 mA (c) 1330 mA (d) 1500 mA.....	48

Figure 34- Nanoindentation hardness profile. .... 49  
Figure A- 1-Hardness profiles in bonded wires with different ultrasonic current with error bars.  
..... 57  
Figure B- 1-880mA Ultrasonic Current with different hold times with error bars..... 58  
Figure C- 1- Nanoindentation hardness profile with error bars..... 59

## **Abstract**

Ultrasonic wire bonding is a critical process used widely across the microelectronics industry. Despite its ubiquity, there is a breadth of literature and ongoing active research into the basic principles of wire bonding. In particular, the effects of ultrasonic bonding on material properties are not fully understood. This thesis presents the effects of different ultrasonic bond powers on material properties. The changes in mechanical properties were measured by collecting Vickers microhardness data and nanoindentation data. The hardness in the bonded wire varied with two parameters: the distance from the bond interface, and the applied ultrasonic power. The hardness varied 5 HV across the profile of a bond and a 5 HV difference was also measured due to change in bond power. In addition, the measured hardness of the bonds was lower by up to 10 HV than calculated hardness values based on strain hardening only. These trends were found with the microhardness data and corroborated by nanoindentation results. This work provides a method to further study the effects of additional bonding parameters on mechanical properties.

# 1 Introduction

Wire bonding is a critical technique used extensively throughout the electronics industry. Despite its widespread usage, the underlying bonding mechanism of ultrasonic bonding is still under active research. One of the key questions is whether ultrasonic bonding results in a hardening or softening effect. Due to the current discrepancies in the literature, a costly and time-consuming “shot gun” approach is used in industry in order to establish viable process parameters. Developing a mechanism and understanding of what processes occur during ultrasonic bonding would lead to better process control and would ameliorate research and development efforts at a lower cost. This would include exploring new wire and substrate materials that are cheaper and/or have better bonding strength and reliability.

Since wire bonding research is closely tied with industrial application, most of the relevant literature focuses on data such as bond strength, fatigue life, and bond time instead of mechanical properties. However, studying mechanical properties further develops a fundamental understanding of the bonding process instead of further optimizing bonding parameters. This would contribute to a stronger foundational knowledge base, upon which both academic and industrial pursuits could be built.

Ultrasonic bonding has numerous parameters such as bond time, and hold time, but the one that is varied throughout this research is ultrasonic power. For this project, analysis is limited to the effect of ultrasonic power to allow for correlations between it and mechanical property changes. Numerous mechanical properties can be measured such as elastic modulus; however, hardness was tested because it can be used to determine material property changes without the complexity that comes with testing other mechanical properties. Hardness is a mechanical

property that is easily measured and can be related to additional mechanical properties such as yield strength, elastic modulus, and strain hardening coefficient.

## 2 Literature Review

Since the early 1980s, wire bonding has been the most used process for joining semiconductors, and is present in over 90% of all bonds in chips [1]. As a result, multiple types of wire bonding have been developed to meet the various demands of industry. The two most common types of wire bonding are ball bonding and wedge bonding which utilize thermocompression, ultrasonic, or thermosonic energy [2]. While a hybrid approach of ball and wedge bonding is commonly used in industry, the focus of this study is the effect of ultrasonic power on mechanical properties, and will thus be limited to ultrasonic wedge bonding [3].

Since the introduction of wire bonding in the electronics industry, researchers have sought to explain the phenomenon. Many attribute Anderson [4] with the first use of wire bonding as a means of connecting electronic leads [4]. Early observations showed that contaminants and oxides are cleaned away from the surface leading to bond formation [5]. According to the early work on ultrasonic bonding, two effects from ultrasonic vibration on mechanical properties are acoustic softening and hardening. In softening, the amount of stress required to achieve plastic deformation is lowered. Langenecker [6] varied the amount of ultrasonic power resulting in an increased and more pronounced hardening effect which was attributed to plastic deformation, [6]. Another early theory for joining was bonding as a thermally activated process [7]. This is corroborated by Krye [8] using transmission electron microscope images, which supported ultrasonic spot welds [8]. Contradicting these findings, thermoelectric electromagnetic field measurements made during ultrasonic welding showed that the maximum temperature achieved did not exceed 40% of the melting temperature and no melting phenomena was seen in cross-section analysis [9]. In addition, Devine [5] demonstrated that the interface does not reach the melting temperatures of the metals and found that

significantly less energy was needed to achieve the deformation due to the presence of ultrasonic vibration—not as a result of the increase in temperature [10]. This data combined resulted in disproving the welding mechanism. After demonstrating that the thermal process of bonding was not consistent with the data, it was accepted that wire bonding is a solid-state process [11].

Table 1 outlines the timeline of key areas of research interest. One useful modern analysis technique that followed the discovery of wire bonding as a steady-state process, is the micro-slip and stick-slip models. This varies from the diffusion theory-based approaches that were prevalent in the 1990s but are still in use today [3]. In micro-slip and stick-slip methods, the interface friction is the key to the joining process [12]. The effects resulting from each mechanism can be described with superposition of stress, increased temperature, dislocation energy absorption, and interface friction [13].

*Table 1-Timeline of key research into bonding mechanisms [14].*

<b>Authors and Year</b>	<b>Method of Research</b>	<b>Reported Mechanism</b>
Langenecker 1966	Experiment	Absorption at dislocations sites and local heating
Izumi et al. 1966	Experiment and Theory	Dynamic stress and heat generation
Baker and Carpenter 1967	Experiment	Mobility of dislocation by thermal activation
Kirchner et al. 1984	Experiment and Theory	Superposition stress
Ohgaku and takeuchi 1987	Experiment	Superposition stress and thermal effect
Malygin 2000	Theory	Oscillatory stress and dislocation motion
Daud et al. 2007	FEM and Experiment	Superposition stress and energy absorption by microstructure
Liu et al. 2013	FEM and Experiment	Superposition stress and dislocation movement and thermal effect

Despite the varied theories and methods described above, many experts agree that at least four steps occur during ultrasonic wire bonding—these include 1) Pre-deformation and activation of ultrasonic vibration, 2) friction, 3) ultrasonic softening and interdiffusion 4) ultrasonic hardening [3], [15]. This thesis will focus primarily on ultrasonic softening and hardening, although all steps are important and under current investigation.

## 2.1 Types of Bonding

The two main wire bonding techniques are ball and wedge bonding. Ball bonding is a thermosonic process because it uses heat and ultrasound to form a bond. It is considered a solid-state process. The main difference between ball bonding from wedge bonding is the formation of the free air ball (FAB) in which the end of the wire in a ceramic capillary is melted to form a ball [16]. The ball is a result of the surface tension of the molten wire. This technique is commonly used with copper wire [2]. The addition of heat introduces metallurgical changes that effect mechanical properties. Figure 1 shows the schematic of a ball bonding capillary and the relevant dimensions. The wire is melted at the end of the capillary and the ball forms. This ball is what is bonded to the substrate.

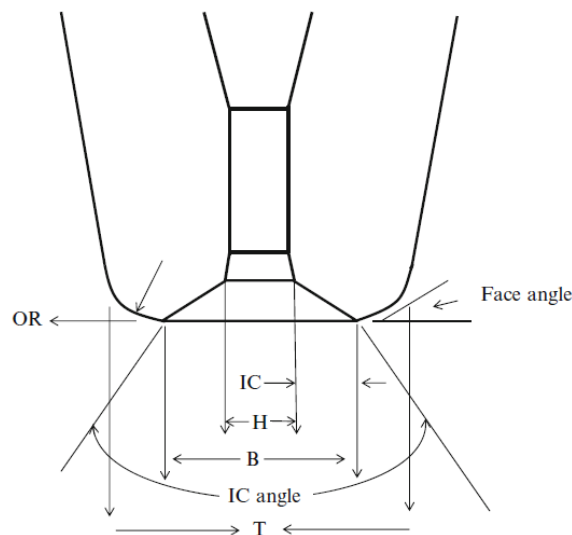


Figure 1- Ball bonding head [2]. Reproduced without permission.

In wedge bonding no additional heat energy is added to the wire. The bonds are formed by a bond head that applies a clamping force normal to the wire as well as ultrasonic vibration longitudinal to the wire [17]. This causes plastic deformation in the wire, bonding it to the substrate. The wire can then be looped, and the process repeated as many times as necessary for

the integrated circuit package [3]. Figure 2 illustrates the direction of the normal force and the tip geometry of a wedge wire bonder. In wedge wire bonding, there are three types of bonds: first bond, stitch bond and end bond.

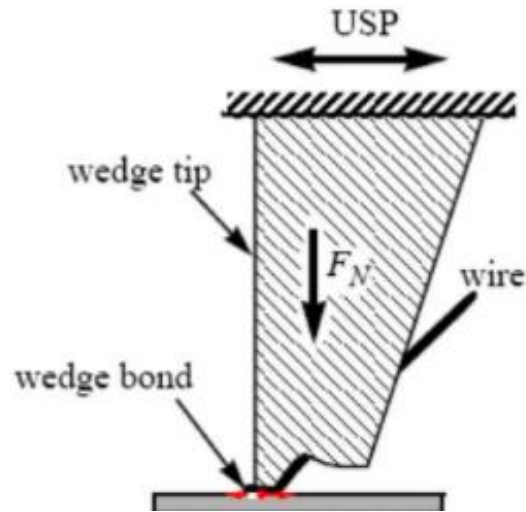


Figure 2- Wedge bonding [17]. Reproduced without permission.

## 2.2 Bonding Parameters and Testing

There are numerous parameters in wire bonding. Each of these parameters needs to be optimized based on the method of wire bonding, wire material, pad material, wire diameter, and desired performance. This optimization process is tedious and requires a large design of experiment to find the appropriate settings [18]. In ball bonding, the contact velocity, initial force, bond force, ultrasonic current, and bond time are the parameters to be optimized. Pull strength, ball shear strength, and cratering performance are commonly used to refine process parameters [2]. In wedge bonding similar parameters to ball bonding are used including: hold time, ultrasonic power, begin-force, end-force, and touch-down steps. Ultrasonic power is one of the most important parameters and requires the most analysis to tune. To analyze the impact of the ultrasonic power on the bond, pull tests, x-ray tomography, and other reliability tests are

performed [19]. The bond strength is the characteristic most related to the mechanical properties of the wire bond. The two tests most commonly used to optimize wire bonding are the pull test and the shear test.

Figure 3 shows pull test results illustrating the different failure modes of the wire bond and the pull strength dependence on ultrasonic power. This pull test was done on 25 $\mu$ m copper wire bonds and demonstrates the relationship between ultrasonic power and bond strength. Insufficient ultrasonic power prevents removal of the oxide layer, resulting in inadequate bonding. However, too much ultrasonic power damages the bonding area [21]. This relationship can be seen in the parabolic curve in Figure 3.

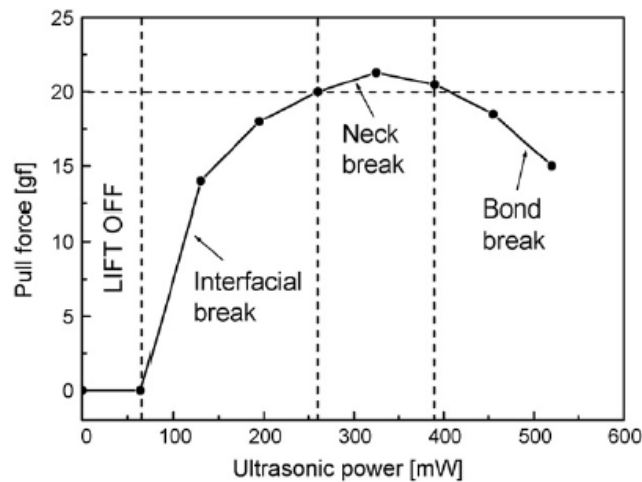


Figure 3- Pull strength vs ultrasonic power [20]. Reproduced without permission.

Another test used to assess bond strength is the shear test. According to experiments in large diameter aluminum wedge bonds, the shear strength also has a parabolic relationship to bond power as shown in Figure 4 [22].

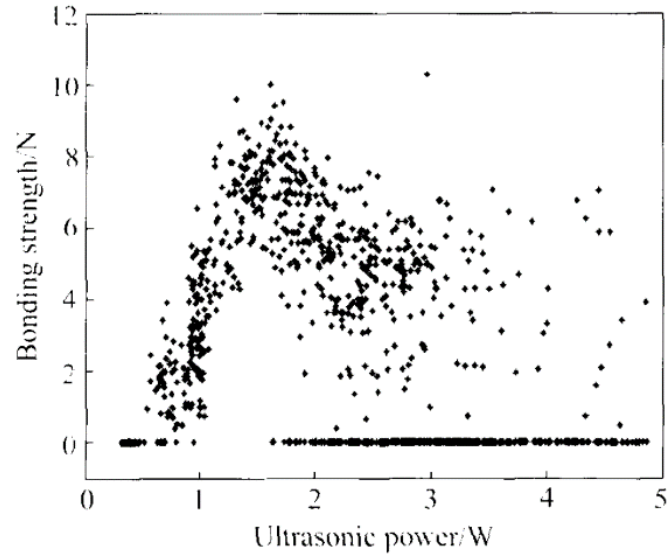


Figure 4- Bond pull strength vs ultrasonic power [21]. Reproduced without permission.

Figure 5 shows a common optimization process conducted for wire bonding using shear tests. In this test, the wires were bonded to a substrate under varying conditions. Following bonding, the wires were then shear tested and the “footprint,” or wire remaining on the substrate, was examined.

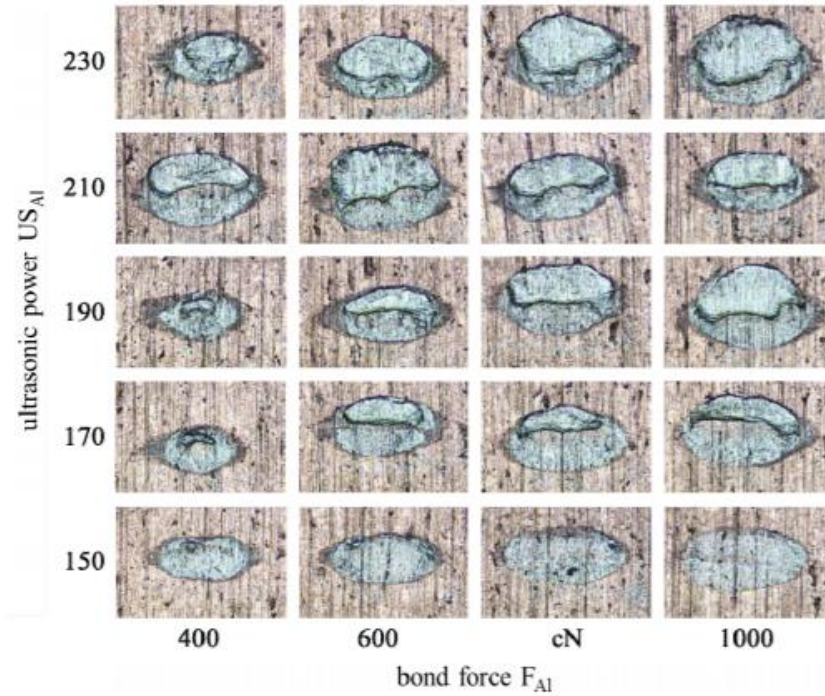


Figure 5- Shear strength optimization for Al wire wedge bonding [23]. Reproduced without permission.

This study was done to compare the process window for copper and aluminum wires. The aluminum wires are shown in Figure 5. The study found that copper bonds had higher pull and shear strength than aluminum bonds. However, copper bonds had a higher sensitivity to operating parameters and higher operating forces, therefore aluminum is regularly used in industrial settings despite its lower strength [23]. The process window for the applied ultrasonic power holds true for other materials and wire diameters [20]. The effect of ultrasonic power on bond strength is closely tied to the changes in mechanical properties and aids in the understanding of the bonding mechanism.

### 2.3 Strain Hardening

Strain hardening, like wire bonding, has unresolved questions in the underlying theory and mechanism. Since the wire bonding process results in deformation of the wire, strain hardening occurs. The extent of the effects of strain hardening are currently being actively

researched. Strain hardening has been divided into 5 distinct stages. Stage I is a single active slip system in a single crystal, stage II is when more slip systems activate, and linear hardening begins. Stage II applies to single and polycrystalline materials. Stage III is the decrease in the work hardening and is sensitive to temperature and strain rate. Stages IV and V consider large strains not accounted for in stages I, II, and III. Stage IV is the gradual increase in hardness at large strains and Stage V is the saturation of the stress. [24]

The important advancements in work hardening involve computational modeling, rather than a theoretical approach. The predominate model is the Kochs-Mecking analysis [25]. The Kochs-Mecking model uses one parameter for the average dislocation density. A constitutive method using Kochs-Mecking model and Levy-von Misses equation has been developed. The model and experimental data confirmed residual hardening and ultrasonic softening.

Microhardness tests also confirmed residual hardening in aluminum increasing from 26 to 34 HV with 100g load and 10 second hold [14].

Figure 6 is the hardness measured with a nanoindenter of an aluminum wire bonded onto a semiconductor chip with a metallization layer. The nanoindentation study of hardness revealed a dependence on distance from the interface. Localized softening can be measured 25  $\mu\text{m}$  from the bonded interface.

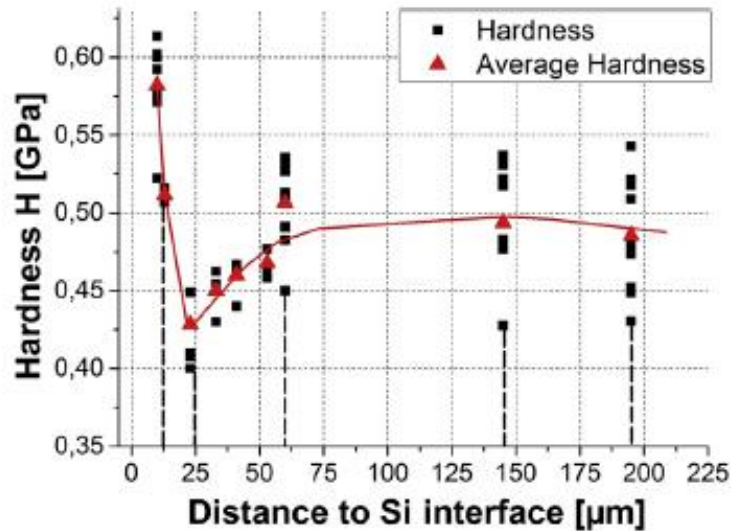


Figure 6- Hardness values obtained by nanoindentation [27]. Reproduced without permission.

However, at the interface and in the bulk of the wire the material has a higher hardness. The hardness variation also aligned with the microstructure changes in the wire, demonstrating the occurrence of recrystallization, recovery, and grain growth, see Figure 7. Figure 6 shows that the hardness measurements are dependent on the distance from the bonded interface [27]. It can also be shown that the time in which the material was subjected to ultrasonic vibration increased the hardness of the wire after bonding, partially due to an increase in the dislocation density increase with exposure time [28], [14].

## 2.4 Microweld Formation

During the initial stages of bonding, microwelds are formed where the wire and substrate create metallic bonds and were first seen in 1984 when the contact resistance of a wire bond was measured[29]. The real time formation of microwelds can be measured using contact resistance measurement techniques. Another method, although potentially less accurate, is with scanning electron microscope (SEM) first used by Seppanen [30]. Laser dopler vibrometry can also be used to see microweld formation occur in wire bonding [31].

## 2.5 Microstructure

Analyzing the microstructure of the wire bonded sample can reveal information about the morphology and material characteristics of a specimen. The microstructure is composed of grains which are the individual crystals that make up a material. The study of grains in metals can be used to track the effect of a process on material properties. The undeformed wire typically has large grains and the bonded wire has substantial amounts of induced defects from the plastic deformation. The result is a fine-grained region with higher hardness [32]. An ultrafine grain structure has been observed after wire bonding in thick aluminum wedge wire bonds on AlSi metalization. In addition, fine nanoscaled grain structure dislocation loops were also observed. The grain structure is stable, however, it has a temperature and time dependence [33].

Small grains of 1  $\mu\text{m}$  or less can be seen after wire bonding. The grains align parallel to the wire drawing direction. The microstructural changes are dominated by dynamic recrystallization and recovery. Certain grain orientations are more favorable for grain growth and energy reduction, which may cause texturing [27].

Figure 7 shows a cross section of an ultrasonic bonded aluminum wire. An inverted microscope with a polarizer was used to show the grain structures.

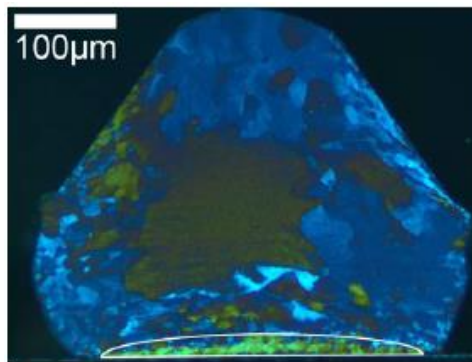


Figure 7- Grain Refinement in Al wire [35]. Reproduced without permission.

At the wire to substrate interface there is a local area of small refined grains. Increasing the bond power expands the grain refinement region [35].

## **2.6 Ultrasonic Softening**

Ultrasonic vibration has a hardening and softening effect. The hardening effects are the result of strain hardening and covered in Section 2.1.3. The softening from the applied ultrasonic vibration allows for the large deformation in the wire to occur—creating the wire bond. The ultrasonic softening effect is a transient effect that occurs during the bonding process. This requires measurements to be taken during the bonding. In situ measurement techniques can be used to understand what is happening when ultrasonic vibration is applied. It allows for direct observation of the phenomena. Vickers indentations taken during ultrasonic vibration show ultrasonic softening by measuring an increase in the diagonal length of indents [36].

Figure 8 shows the stress-strain curve from an ultrasonic vibration compression test. A cylindrical compression specimen is subject to ultrasonic vibration as a compression load is applied the stress and strain is measured. The in-situ compression tests showed significant softening of materials from high-frequency vibration. [28].

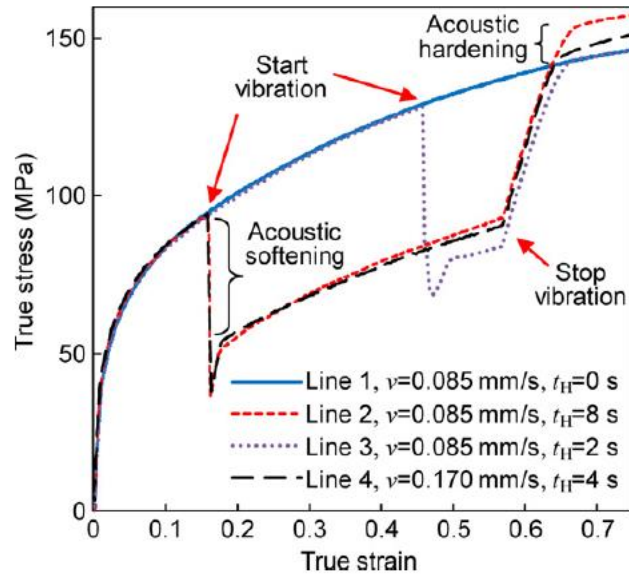


Figure 8- Stress-strain compression tests with and without high-frequency vibration [28]. Reproduced without permission.

While the transient softening effects are apparent from the in-situ measurements, Figure 8, the residual hardening effects are less conclusive. The literature in Section 2.1.3 shows evidence of an increase in residual hardness with higher bond powers. However, some literature shows that the microhardness decreases with increasing bond power, Figure 9. A linear relationship between microhardness and deformation was also found, Figure 10. This data supports the conclusion that ultrasonic softening is reducing the amount of strain hardening because a larger deformation should result in higher hardness, contradicting other data in literature [37].

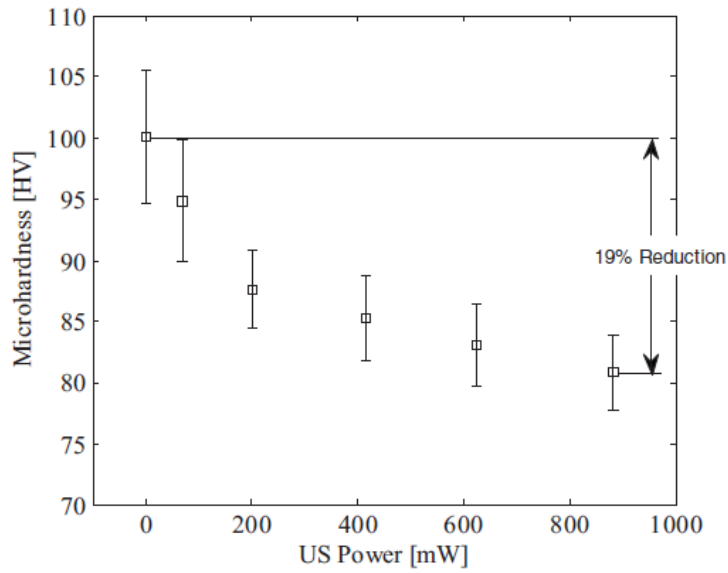


Figure 9- Microhardness of Cu balls deformed with different US [37]. Reproduced without permission.

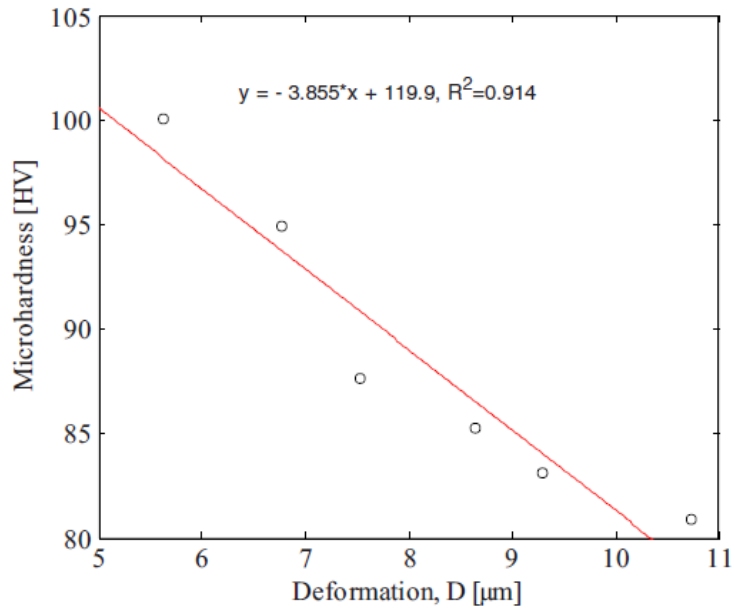


Figure 10- Correlation between microhardness and additional deformation [37]. Reproduced without permission.

## 2.7 Nanoindentation

Nanoindentation is a technique that was developed by Oliver and Pharr [38] in 1991 that commonly uses a Berkovich indenter to determine hardness and elastic modulus of materials. Unlike microhardness tests, nanoindentation measures the interaction between load and displacement. A loading profile is used to control the applied load over the time of test. The result of the loading over time is a load displacement curve. The height of the indenter is measured and used to determine displacement. The load displacement curve is used to calculate the hardness and reduced modulus of the sample. The strain hardening exponent and yield strength can also be calculated using indentation data [39], [40].

$$\frac{1}{E_r} = \frac{(1 - \nu^2)}{E} + \frac{(1 - \nu_i^2)}{E_i} \quad (1.1)$$

where,  $E$  is the elastic modulus of the sample,  $\nu$  is Poisson's ratio of the sample,  $E_i$  is the elastic modulus of the indenter,  $\nu_i$  is the Poisson's ratio of the indenter, and  $E_r$  is the reduced modulus measured by the nanoindenter. The stiffness is the slope of the unloading curve and is used to find the  $E_r$ . In order to find the slope of the unloading curve, a power law fit is applied [38].

The nanoindentation process is highly sensitive and important considerations must be taken when performing a test to ensure the quality of the data. The test method is sensitive to sample surface finish, tip geometry, and sample material. The process requires a more polished surface than typical hardness testing such as a Vickers microhardness test. Nanoindentation also utilizes and relies on experimental values to determine attributes such as indenter shape and indenter deformation. The Berkovich indenter is a triangular pyramid indenter and the process is highly sensitive to indenter shape and must be calibrated [41]. When performing nanoindentation

it is important to consider the deformation around the indent, which is the nonuniform sink-in or pileup around the contact area. This can be a source of error in the measurements. The sensitivity of nanoindentation was evaluated using finite element analysis, as a result of the study pileup was found to be a significant factor when  $h_f/h_{max} > 0.7$  (where,  $h_f$  is the final displacement, and  $h_{max}$  is the maximum depth of the indenter) and the material does not significantly strain harden [42]. The strain hardening rate and ratio of yield stress to elastic modulus are the dominant properties that effect contact depth and projected area [43].

## 2.8 Relationship Between Hardness and Mechanical Properties

The ability to correlate hardness with other mechanical properties is a valuable tool in studying wire bonding. There is a significant experimental effort to relate hardness to different mechanical properties such as tensile and yield strength. Linear relationships between hardness and yield strength can be determined via experimentation [44], [45], [46]. The ultimate strength can be related to the hardness of a material.

$$\sigma_u = \frac{H}{2.9} [1 - (m - 2)] \left[ \frac{12.5(m - 2)}{1 - (m - 2)} \right]^{(m-2)} \quad (1.2)$$

$$n = m - 2$$

where,  $m$  is the Meyers coefficient,  $n$  is the strain hardening coefficient,  $H$  is the diamond pyramid hardness of the material, and  $\sigma_u$  is the ultimate strength of the material [47]. The more commonly used form is the approximation of the Equation 1.2 found in Equation 1.3.

$$\sigma = K\epsilon^n \quad (1.3)$$

Where  $n$  is the strain hardening coefficient,  $\sigma$  is the stress,  $\epsilon$  is the true strain and  $K$  is a constant. Hardness testing, especially nanoindentation, can be employed to determine  $n$  and  $K$ . Using these values, the strength can be estimated. In addition, experimental data has shown a linear relationship between the hardness value and strength. As a result, measuring changes in hardness implies a direct change in strength [48].

Figure 11 shows comparison between experimental tensile strengths and predicted tensile strengths based on their hardness. This experimentally supported relationship was able to predict the tensile strength in aluminum.

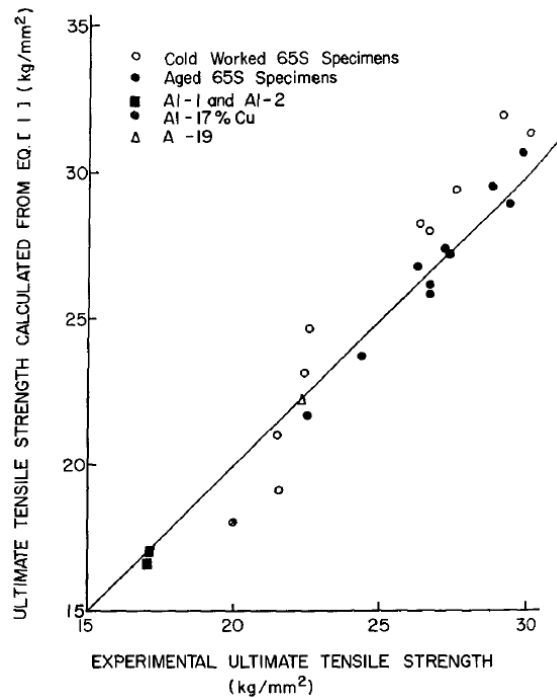


Figure 11- Comparison of calculated and experimental tensile strength for Al alloys [48]. Reproduced without permission.

However, the results can vary between microindentation results and nanoindentation tests as well as between tensile and compression tests. This is because the size of the grains compared to the indent can impact the validity of the test. Another method to study mechanical properties

is a microcompression test performed on the bonded wire instead of hardness testing. It has been shown that microcompression tests align with known tensile strengths better than ones derived from microindentation tests but are more difficult to perform [49].

### 3 Methodology

#### 3.1 Wire Bonding

An Othodyne 7600HD wirebonder was used to prepare all the samples tested. The wirebonder used to make the samples is presented in Figure 12 showing the bond head, sample holder, reel of wire, and computer to control the machine. Aluminum wire with a diameter of 0.02” (508 $\mu$ m) 99.99% pure aluminum was used. The substrate that the wires were bonded to was 5052-H32 aluminum.



*Figure 12- Othodyne 7600HD wirebonder.*

An example of a sample with the wires bonded onto the substrate is shown in Figure 13. The substrates were placed into an alignment jig during bonding so that bonded wires would be in consistent locations for sample preparation. The initial wire bonding process parameters were provided by an industry partner Kuliche and Soffa.

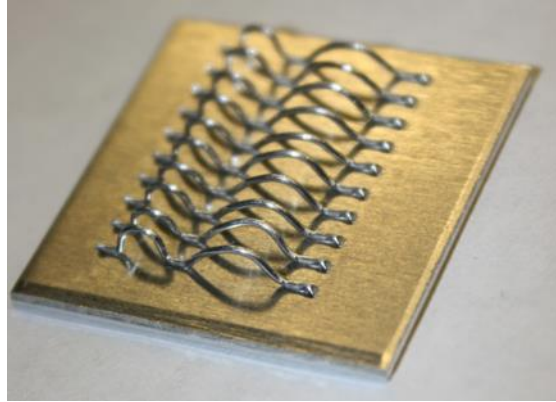


*Figure 13- Wires bonded to substrate.*

The parameters were further optimized for the wire and substrate materials. The parameters were optimized for bond strength and longevity. The parameters are listed in Table 2. The process parameters were varied in sets of single variable experiments. The resulting bonding current based on bond power setting are plotted in Figure 14 and enumerated in Table 3.

*Table 2-Key bonding parameters.*

Touch Force (N)	Start Force (N)	Bond Force (N)	Start Power	Bond Power	Start Ramp Time ( $\mu$ sec)	Bond Ramp Time ( $\mu$ sec)	Bond Hold Time ( $\mu$ sec)
1000	1200	1440	105	130	20	25	155

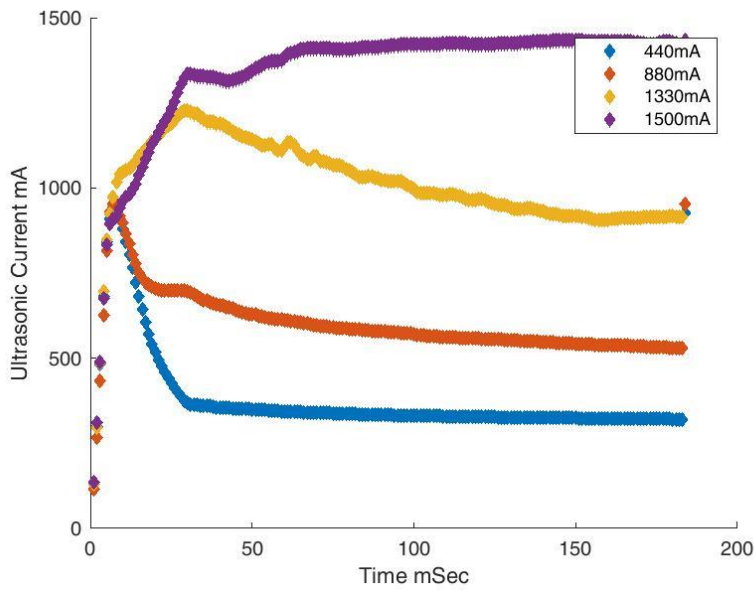


Figure 14- In Situ bonding current for different bond power settings.

Table 3-Relationship between bond tool setting and Ultrasonic Current.

Bond Tool Setting	75	150	225	255
Ultrasonic Current (mA)	440	880	1330	1500

The bonding tool does not set bonding power or current explicitly. A parameter from 0-255 was used. Four bonding power settings were tested and the steady state current was recorded, Figure 14. The data in Table 2 allows the bond power to be reported in an ultrasonic current, not in the arbitrary units used in the machine computer interface.

It is important to note that in Figure 14, the ultrasonic current for the lower bond power settings, 75(440mA) and 150(880mA), exceeds the steady state value. This is in part because the start power was set higher than the hold bonding power, Table 2. The curves above in Figure 14 are an example of the ultrasonic current during the bonding of four individual bonds. The

software adjusts the current to maintain deformation calculated by measuring the height displacement.

### 3.2 Sample Preparation

The samples were mounted in acrylic epoxy, cross-sectioned, and then polished. The uniformity in sample preparation was important to get consistent results across the tests. The polishing preparation can affect hardness testing data because surface roughness can skew the testing, especially nanoindentation, microhardness testing is less sensitive.

#### 3.2.1 Mounting

Samples were mounted in acrylic to prevent damage to the delicate wirebonds during cross-sectioning and polishing. Samplkwick from Buehler was used as a mounting epoxy. The samples were cured for 15 minutes in 1.25 inch sample molds.

#### 3.2.2 Cross Sectioning

A diamond saw was used to cross-section the samples to remove enough material to allow for grinding and polishing to reveal the bonded surface. Figure 15 shows the saw and sample placement.

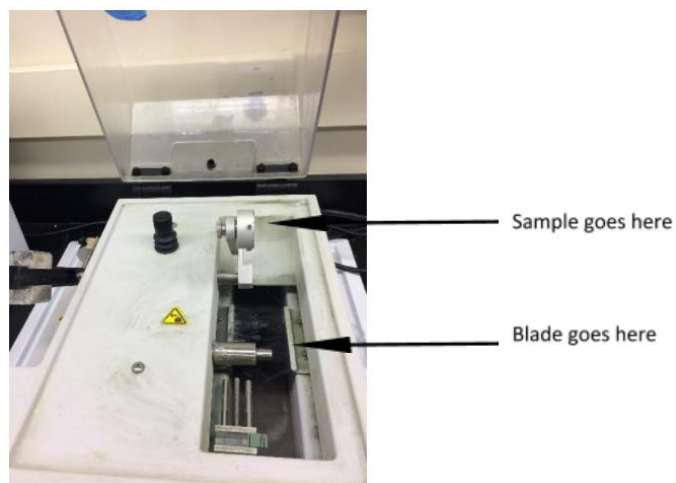
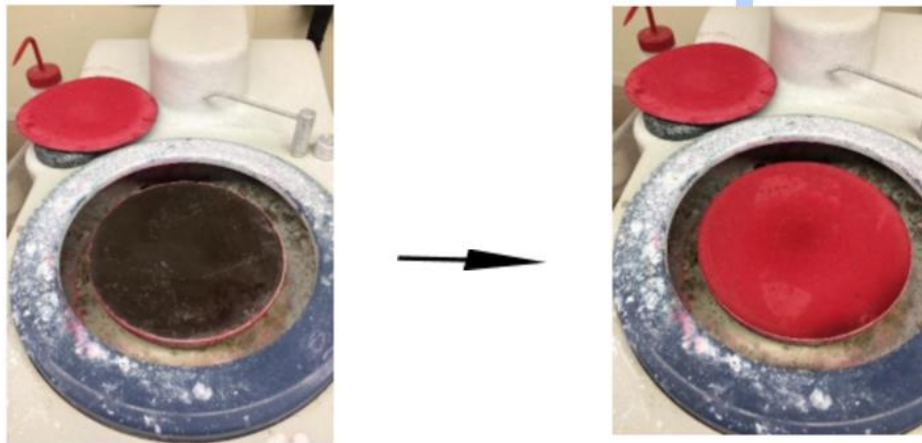


Figure 15- Diamond cross-sectioning saw.

The saw was run at 175 rpm. It was only for coarse material removal. Orienting the sample properly in the saw ensured that the sample was not cut at an angle, causing the exposed bonded area from polishing to be skewed.

### 3.2.3 Polishing

The sample preparation was completed by polishing the surface to allow for consistent hardness testing. The samples were ground with progressively finer sand paper from 240 grit to 600 grit. Then the samples were polished on a polishing wheel. The polishing pad was replaced for each size of polishing solution to prevent contamination, Figure 16.



*Figure 16- Polishing wheel.*

Polishing solution was added to a reusable polishing pad (magnetically attached to the wheel) in order to polish each sample. The polishing solution was made by mixing alumina powder with distilled water. Alumina powder with particle sizes of 5  $\mu\text{m}$ , 1  $\mu\text{m}$ , 0.3  $\mu\text{m}$  and 0.05  $\mu\text{m}$  were used. The final polish was done with 0.05 diamond suspension. For the samples that were tested with nanoindentation, a cleaning step was also performed after polishing. The samples were cleaned in an ultrasonic bath with isopropyl alcohol (IPA). Following, a magnetic disk was glued to the bottom and sanded flat to allow the sample to be mounted onto the nanoindenter's magnetic base.

### 3.3 Microindentation

There are numerous experimental techniques that have been developed to measure the hardness of a material. The hardness of a material is its resistance to abrasion and penetration. Hardness testing techniques can be classified by the geometry of the indenter: ball, cone, sharp diamond, or pyramid. All these techniques rely on applying a known load to form a measurable indent in the material. The three most common indentation techniques are Knoop, Vickers, and Brinell [44].

The Vickers hardness measurement was selected for this study because it uses the same indenter for all materials and can accurately produce small indents. Vickers hardness was developed in 1921 at Vickers Limited. Smith and Sandland [44] wanted to find a replacement for the Brinell testing method [44]. The first tests used diamonds of non-standard shape, but now the shape of the indenter is standardized by ASTM E384 [50]. The indenter for the Vickers test is a square-based pyramid with  $136^\circ$  face angle. The indenter is composed of diamond. The Vickers hardness tester is illustrated in Figure 17. The stage, sample holder, and optical port are pictured.

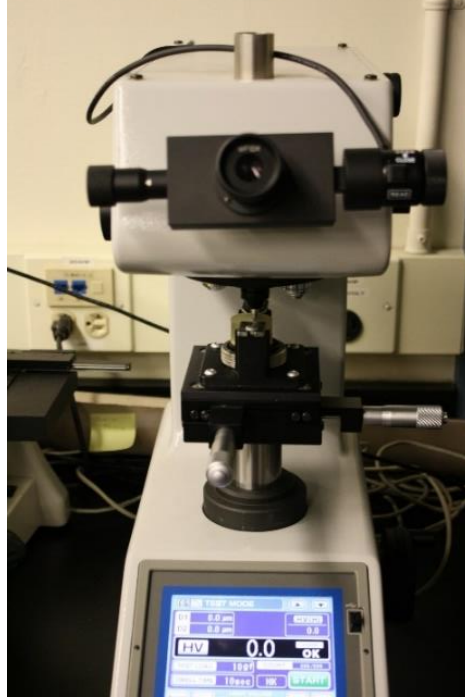


Figure 17- Microhardness tester.

The hardness is calculated by applying a known force and calculating the surface area of the indent. The mean of the two diagonal lengths of the indent are used to calculate the surface area.

$$HV = \frac{\text{Test Force}}{\text{Surface Area}} = 1.8544 \frac{F_{(kgf)}}{d_{(mm)}^2} \quad (2.1)$$

The variable, F, is the load the indenter applies to the sample, the diagonal average of the two diagonal lengths, d, is used to calculate the surface area of the indent formed by the specified loading force [51]. The surface area of the indent scales inversely proportionally with the applied load.

The loading force for the Vickers hardness measurements was established. Samples were cut, polished, and mounted in the Leco microhardness tester. A series of indents were made using different loading forces, 5gf to 2kgf. The smallest loading force that was able to make reliable indents was selected—10gf. Once the loading force was selected, the size of the indent

was measured. The maximum diagonal length was measured to be 19  $\mu\text{m}$ . A spacing of 75  $\mu\text{m}$  was used between all the indents. This placed all indents four times the diagonal distance away from any other indent. This was done to prevent strain hardening from previous indents influencing new samples, due to close proximity. The samples were aligned in the indenter, so the hardness measurements were taken orthogonal to the wire substrate interface, which was important to collect consistent data points.

### **3.4 Optical Microscopy**

An optical microscope was used to inspect the samples and take a picture of the indents for later analysis. The microhardness tester has its own microscope, but has a smaller field of view and lacks a camera. A Leco microscope with 5x, 10x, 20x and 50x objective lens was used for image analysis. Once the loading force from Section 3.3 was selected, the indents were observed at different magnifications. For post-processing later, it was critical to get contrast between the indent and undeformed wire. At 20x magnification, the contrast was determined to be the best for image analysis because the entire wire could be seen in a single image and did not require multiple pictures that needed to be stitched together.

Once the proper magnification was chosen, the microscope had to be calibrated to ensure accurate results. The microscope was calibrated using a calibration slide and calibration software built into the Leco software tool. Once the calibration was performed, the calibration and image analysis techniques detailed in Section 3.4 were validated by measuring known various features on the calibration slide. The slide had a cross hair with 0.01mm divisions, a cross hair with 0.1mm divisions, 0.07mm diameter dot, and 0.015 diameter dot. Figure 18 shows the image analysis determined length of specific features on the calibration slide. A linear fit was used to compare the actual distance values with the measured values.

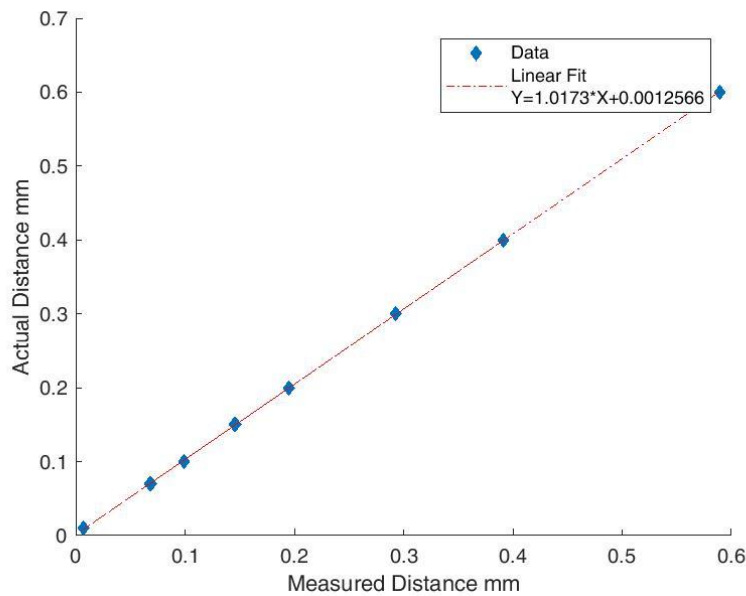


Figure 18- Comparison of calibrated microscope measurements to actual measurements.

The linear fit has a y-intercept of 0.0013. A small y intercept means that there is no fixed bias between the two sets of values. The slope of the line is 1.017. This indicates that the measured distance is 1.7% smaller than the actual distance. This was consistent for all the measured distances, short and long. With the microscope calibrated and image analysis validated, the data could be collected with high certainty.

### 3.5 Image Analysis

To process data faster and more reliably, an image analysis script was written in MATLAB included in Appendix D. The script uses a picture of the indents from the microscope and finds the position of the indents to calculates the hardness. A scale bar was included in the pictures taken on the microscope to be used as a conversion between pixel size and actual length in  $\mu\text{m}$ .

To perform the microhardness measurements, image analysis is common to eliminate the human error from manually measuring each indent. For the measurement to be made, an optical

microscope image was converted to a black and white binary image. This is known as binarization [52]. Objects in the binary were analyzed using canny edge finding and compared against a criteria based on object attributes to find indents [53], [54], [55], [56]. The process for the image analysis script is listed below and illustrated in Figure 19. The process was implemented in MATLAB.

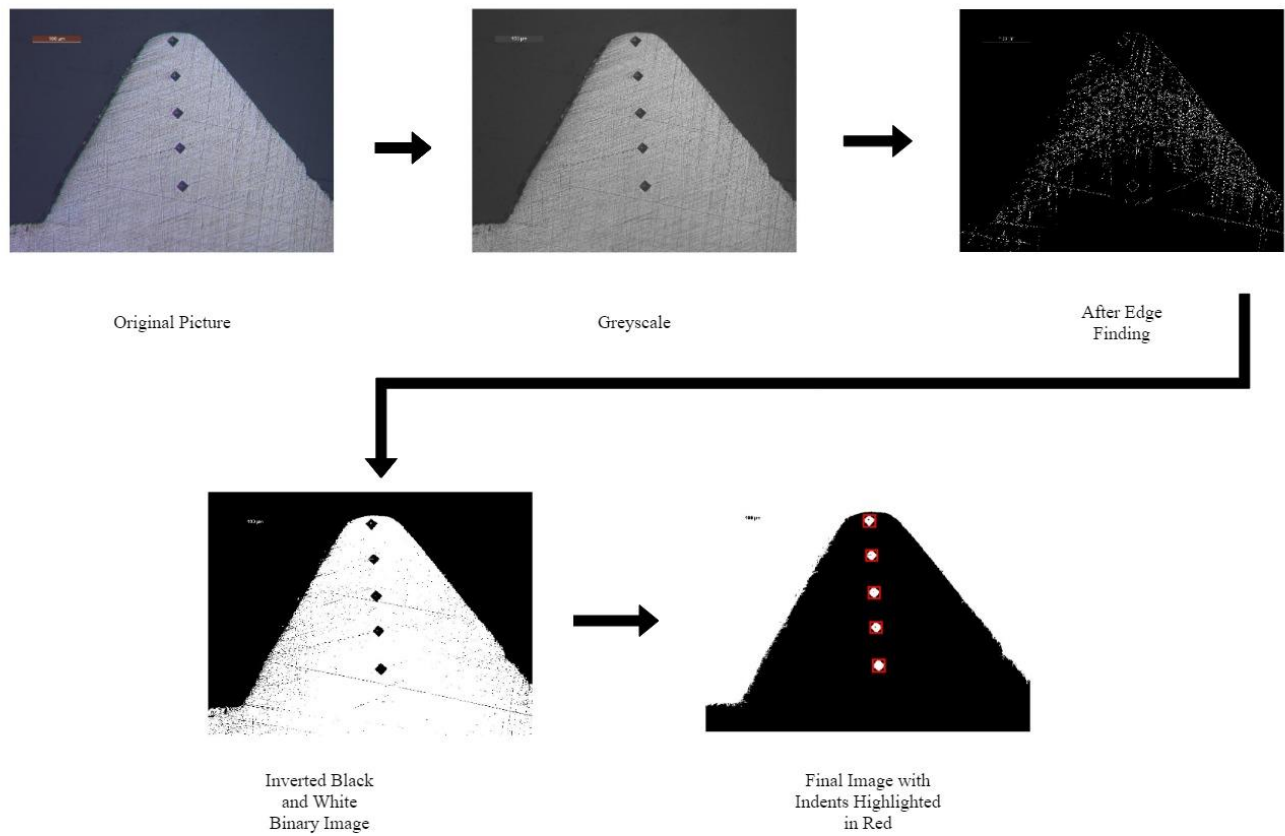


Figure 19- Image analysis diagram.

Figure 19 illustrates the different stages in order to calculate the Vickers hardness from a microscope image. To process the image, key attributes of the scale bar and indents were determined. These attributes made it possible to filter the image and ensure only the indents were read. It also guaranteed the correct scale bar length was used. The scale bar was a long, thin,

uninterrupted rectangle. It was consistently the same width. The scale bar was found by searching for a 3 to 6 pixel wide bounding box of over a length of 200 pixels after running the canny edge finding algorithm. The edge finding algorithm locates edges and was readily able to find the scale bar.

To filter the images, the objects within the image were compared against two criteria: ratio of diagonals and object size. The indents should have nearly square bounding boxes because the diagonal lengths should be similar in length. Small image artifacts were filtered out because the indents have an area larger than 400 pixels. The squareness of the potential indent was determined by the ratio of the bounding box dimensions. The bounding box dimensions are the lengths of the diagonals. When the ratio of indent diagonals was larger than 0.875 and smaller than 1.125 the image artifact was considered an indent. The criteria was determined by measuring the diagonal length of a series of indents and determining the ratio for those indents. The ratio of the indents was found to be 0.975 to 1.025. A factor of 0.1 was added to ensure that the program errored on the side of including an indent which could be manually removed after inspecting the results. This filtering criteria also made sure that non-square indents were ignored as they are not valid hardness measurements. The process for the image analysis script is listed below and illustrated in Figure 19.

In order to validate the image analysis software, a series of indents were made into an unbonded wire. The indents were measured manually on the indenter and then compared with the results from the image analysis software. The manual method measured an average of 25.57 HV with a standard deviation of 0.97, while the image analysis software measured an average of 32.52 HV with a standard deviation of 2.01. The higher reading from the image analysis is consistent with the known error in the image analysis tool. The smaller deviation in the manually

obtained measurement could also be a bias introduced during the process. The image analysis method was selected because it can be used to measure relative changes across the samples without introducing bias and can process samples more quickly.

### 3.6 Nanoindentation

A Hysitron nanoindenter was used to perform more precise indents to obtain a better resolution of the hardness profile within the wire. The interior of the nanoindenter is shown in Figure 20. The indenter, transducer, stage, sample mount, and microscope are pictured.

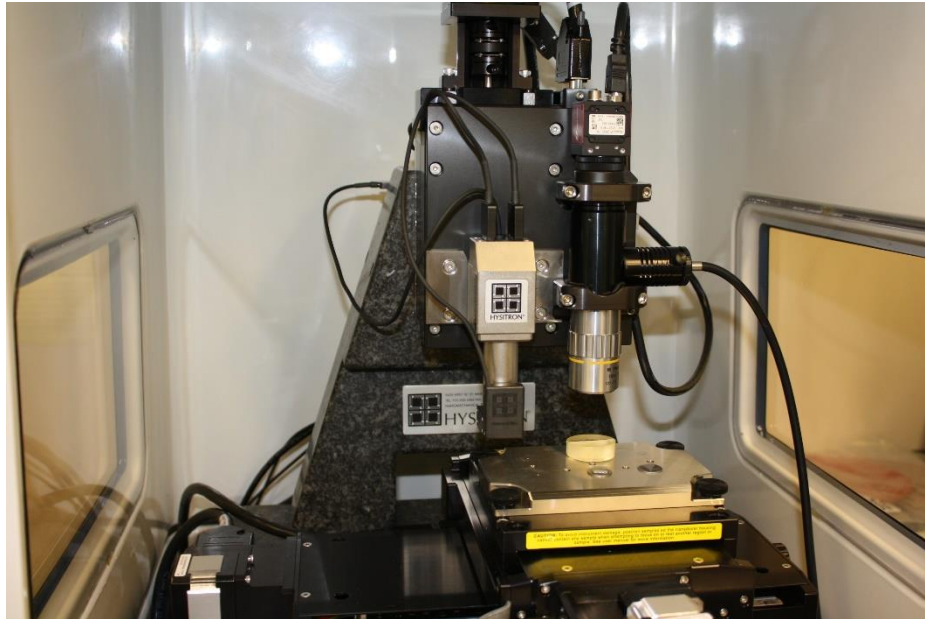


*Figure 20- Inside of nanoindenter with sample.*

Once the sample is placed within the tester, a sample region can be created and the location for each indent set. Unlike the microhardness tester, which was operated manually, the nanoindenter is fully automated. A loading profile must be selected for the specified indent location. There are single and multiple loading profiles. The single loading profile can have a dynamic or constant load (such as the trapezoid profile pictured below). Figure 21 illustrates a trapezoidal loading profile.

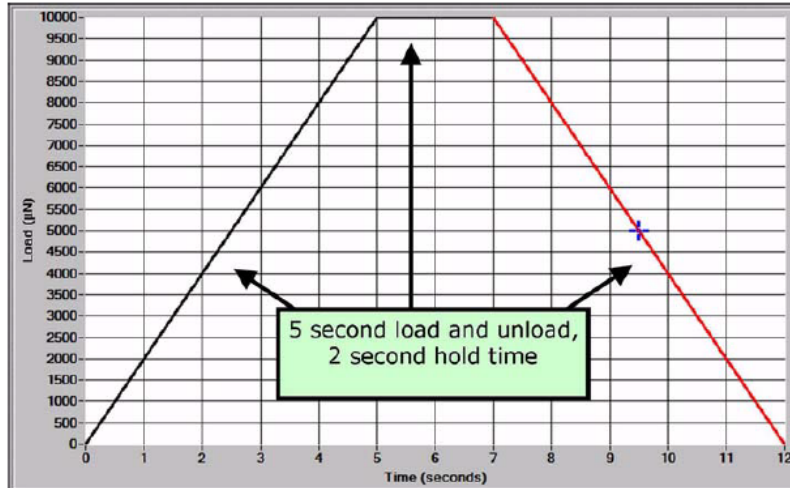


Figure 21- Quasi Static Trapezoid [57]. Reproduced without permission.

The peak load can be set in mN. Hold time and ramp time were set in seconds to create the loading profile. An application within the software tool to run the nanoindenter from Hysitron allowed for the creation of custom loading profiles, including multiple loading. The multiple unloading profile allows for the collection of multiple data points at a single indent, Figure 22. It also collects data at multiple loading forces. The multiple unloading profile was the preferred method because it could collect data more quickly [57].

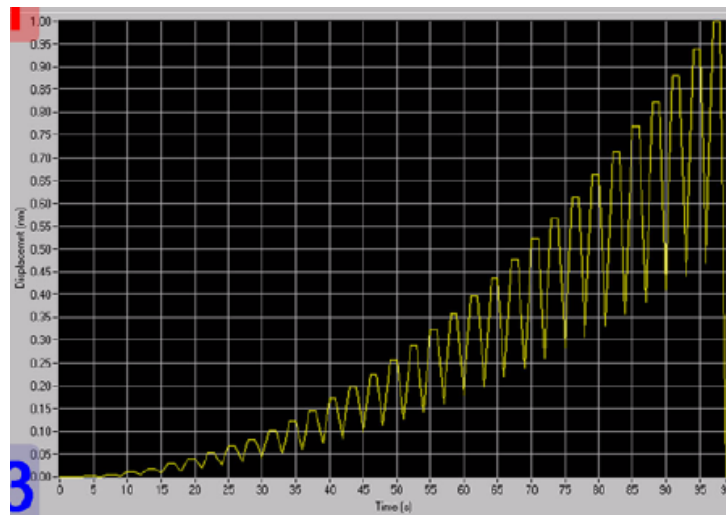


Figure 22- Partial Unloading profile [57]. Reproduced without permission.

Before use, the multiple unloading method was tested by comparing the hardness measured at 3500 mN to 10000 mN loading force with 500 mN intervals from single unloading tests. A multiple unloading test was performed using 3500 mN to 10000 mN loading force with 500 mN intervals. The multiple unloading testing is different because at each indent the entire range of loading force was tested instead of a single indent being needed for each loading force. The hardness was compared between the two tests and the minimum loading force for consistent hardness results was found and shown in Figure 23.

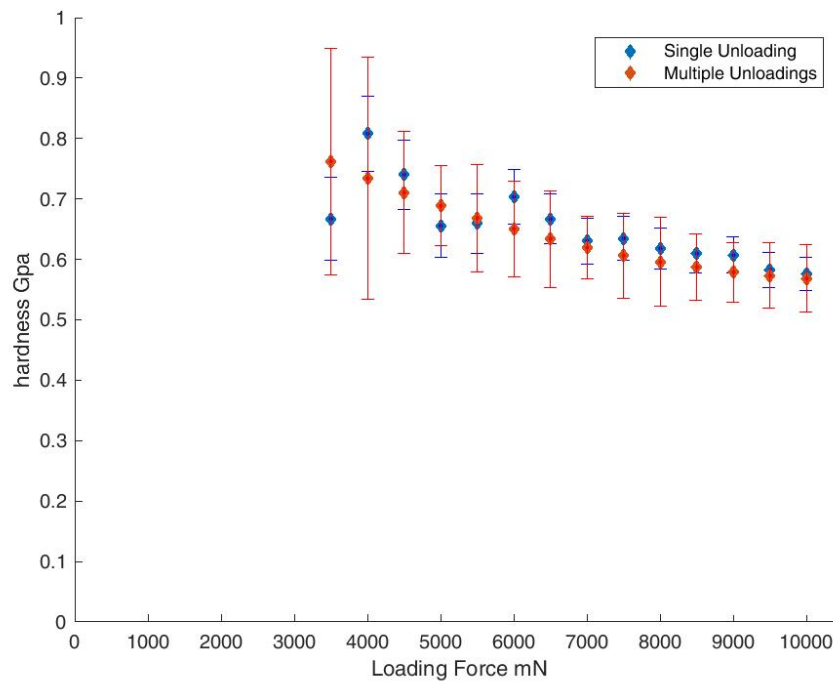


Figure 23- Load force vs hardness for single and multiple unloading testing.

Indents were performed in the substrate, Figure 23, using the single and multiple unloading technique described above. The data shows strong agreement between single and multiple unloading tests. This justifies the use of the multiple unloading method for data collection. There

is a dependence between the loading force and hardness. The data is consistent at loading forces above 4.5 mN. As a result, 4.5 mN was used as the minimum loading force.

## 4 Results and Discussion

### 4.1 Microindentation

Before collecting data on the effect of ultrasonic power on mechanical properties, two samples were tested with different cross-section orientations. The results are reported in Table 4. There are two directions the wire could be sectioned, longitudinal and transverse, as shown in Figure 24. The values from the transverse and longitudinal data were subtracted from each other to calculate the variation between the two cutting directions. This initial test was run to find the optimal method to orient the wire for sample preparations, as well as eliminate any sources of errors introduced by the orientation of the wire.

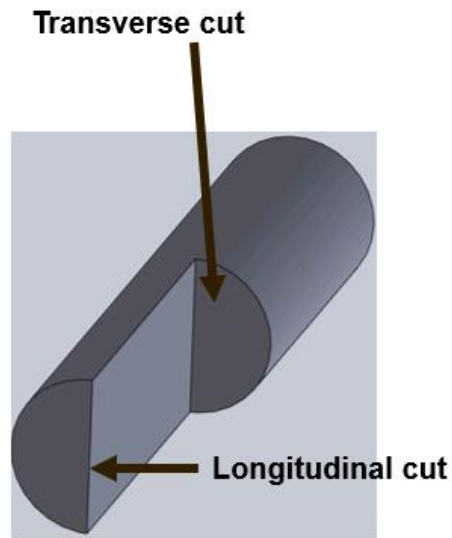


Figure 24- Orientation of Wire Cross Section.

Table 4-Hardness orientation data

Distance From Interface ( $\mu\text{m}$ )	Longitudinal Hardness (HV)				Transverse Hardness (HV)				Longitudinal-Transverse (HV)			
	440 mA	880 mA	1330 mA	1500 mA	440 mA	880 mA	1330 mA	1500 mA	440 mA	880 mA	1330 mA	1500 mA
375	31.12	35.56	37.70	34.37	35.98	35.35	36.27	41.56	-4.85	0.21	1.43	-7.19
300	37.26	37.70	35.56	33.98	36.82	38.37	38.32	34.58	0.43	-0.67	-2.76	-0.60
225	33.98	36.40	35.56	34.76	34.76	36.49	38.31	36.12	-0.78	-0.10	-2.75	-1.36
150	35.56	33.61	33.23	31.46	31.81	37.58	37.49	37.67	3.76	-3.98	-4.26	-6.20
75	34.76	32.87	32.15	36.82	32.87	32.07	34.05	33.16	1.89	0.80	-1.90	3.66

It was determined from the data in Table 4 that there was not a significant difference between the transverse and longitudinal cut samples. Indents on the longitudinal cut sample had a higher hardness, but within the expected error of the measurement. While it was determined to not be a significantly impactful variable, for consistency, all the data collected and presented in this report was done with transverse cut samples. This was selected because the transverse orientation provided a larger window to cut samples.

## 4.2 Wire Deformation

During the bonding process, the wire undergoes plastic deformation, as schematically shown in Figure 25.

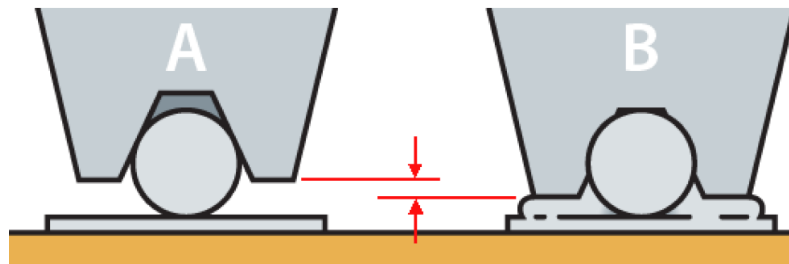
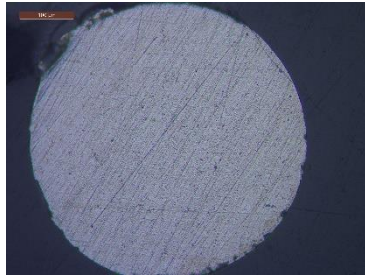
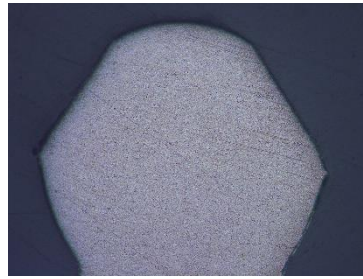


Figure 25- Schematic of bond tool and deformed wire [57]. Reproduced without permission.

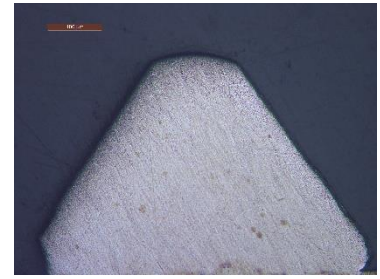
The deformation is a result of the normal force being applied, shown in Figure 25, and the softening from the applied ultrasonic vibration. The normal force was held constant during this testing. It is expected that higher ultrasonic power (which is controlled through the ultrasonic current applied to ultrasonic transducer in the bonder) would result in more deformation. The higher bond currents did in fact lead to higher amounts of plastic deformation. Figure 26 shows the increase in wire deformation as the ultrasonic power is increased, while holding the normal force constant.



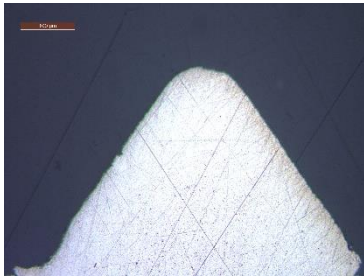
(a) unbonded



(b) 440 mA



(c) 880 mA



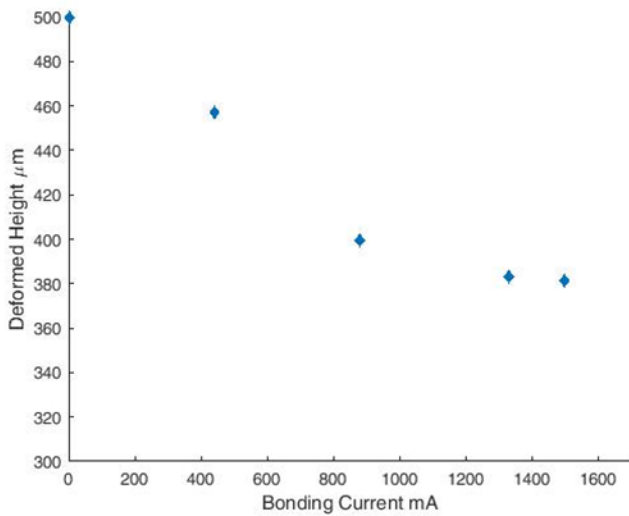
(d) 1330 mA



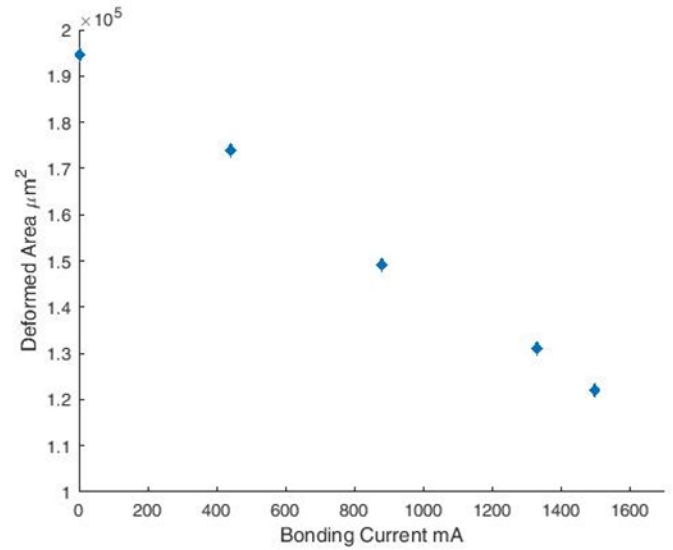
(e) 1500 mA

*Figure 26- Cross-section of bonded wire at varied ultrasonic currents, (a) unbonded, (b) 440 mA, (c) 880mA, (d) 1330 mA, and 1500 mA.*

The unbonded wire was round, but the wire progressively takes the shape of the bonding tool as the ultrasonic current is increased. The height of the wire is decreased until it completely takes the shape of the bond tool and no more deformation is possible. The wire deformation was measured in two different ways, height, and change in cross sectional area, shown in Figure 27.



(a)



(b)

Figure 27- (a) Wire height vs bonding current and (b) deformed cross-sectional area vs bonding current.

The change in cross-sectional area was linear with bonding current, Figure 27(b), but the irregular shape, Figure 26, of the deformed wire makes it inconclusive. The height data, Figure 27(a), was considered more reliable since it is used by the wire bonder to control the bonding process. However, no statistical analysis was done on the wire height or deformed area data since only one set of data was collected.

The deformed height was used to calculate an expected hardness of the wire from strain hardening only. The theoretical hardness calculated is listed in Table 5 along with some of the intermediate values used to calculate the final theoretical hardness.

Table 5- Bond area and calculated hardness.

Bond Power (mA)	Bond Area (pixels <sup>2</sup> )	Bond Area (μm <sup>2</sup> )	Hardness (HV)
0	2912609	194544	33.67
440	2600000	174000	42.02
880	2220000	149000	44.06
1330	1960000	131000	44.46
1500	1830000	122000	44.5

The image analysis software was used to calculate the area of the bonded wire in terms of pixels, Table 5. The scale bar in the image was measured and used to convert the area in terms of pixels<sup>2</sup> into area (μm<sup>2</sup>). The area was normalized and used in Equation 1.3 to calculate the hardness.

$$\sigma = K\epsilon^n \quad (1.3)$$

A strain hardening exponent, n, of 0.25 was used and a K of 2.9 was used to determine the theoretical hardness. The theoretical hardness calculated in Table 5 was compared to experimental data in Figure 28. The actual hardness was taken at 150 μm from the interface, Figure 29. The expected hardness was higher than the measured hardness. This implies there is a combination and interplay between strain hardening and ultrasonic softening.

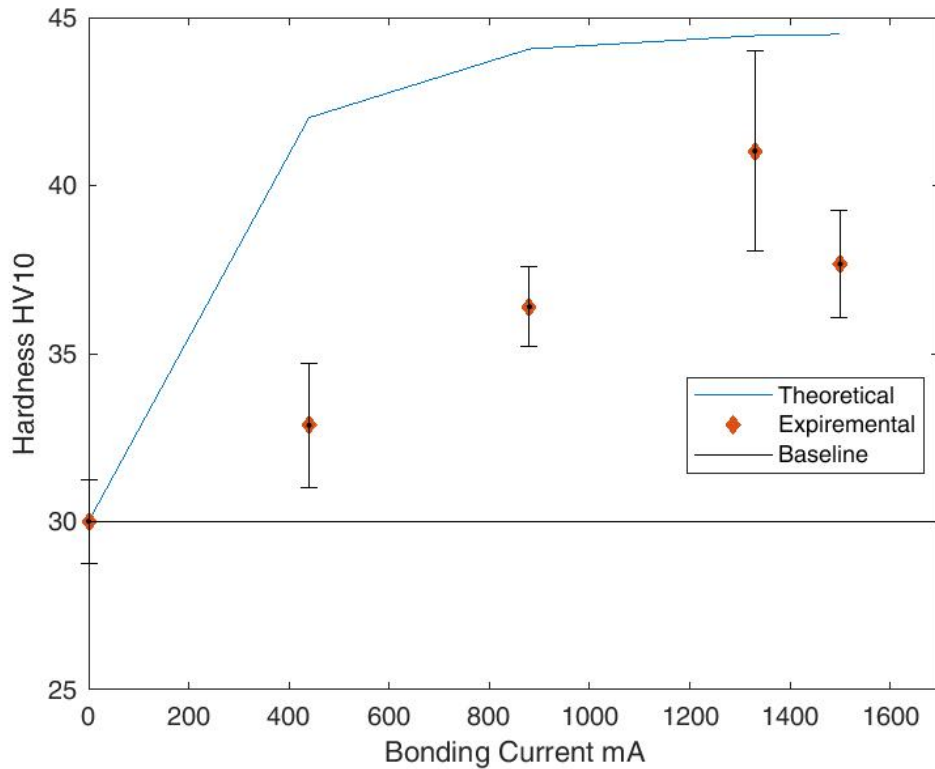


Figure 28- Comparison of actual and theoretical hardness.

A baseline was established by mounting unbonded wires and following the process in Section 2 to measure the hardness using Vickers microhardness testing. The unbonded wire was found to have a hardness of 31.1 HV and is included in the microhardness data as a reference. It is the hardness of the wire before it has been ultrasonically bonded to the substrate. The location of peak hardness was found to be at 150  $\mu\text{m}$  from the interface, Figure 29. It is the value at 150  $\mu\text{m}$  from the interface that was reported in Figure 28. A higher hardness in the middle of the wire was unexpected. It was anticipated that the ends of the wire (which see the highest amount of deformation) would have the highest hardness. However, the spacing of indents for microindentation was placed away from the initial strain hardened region.

#### 4.2.1 Power Dependence

As mentioned above, the wire deformation variation was because of the ultrasonic current applied. There was also a resulting hardness profile in the wire, the hardness varied with distance from the interface. The hardness profile in the wire was also dependent on the ultrasonic current applied. Samples were prepared using the values in Table 2 while varying ultrasonic current. Their hardness was measured and reported in Table 6.

*Table 6- Hardness in HV measured at different locations in wire and at varied bond currents.*

Distance from Interface ( $\mu\text{m}$ )	Bond Current			
	440mA	880mA	1330mA	1500mA
375	35.98	37.7	37.97	37.26
300	36.82	39.55	39.79	34.58
225	34.76	38.61	38.4	36.12
150	31.81	36.4	41.03	37.67
75	32.87	35.16	35.77	33.16

The image analysis software was used to collect the data. A sample at each bond current was prepared and analyzed following the procedure in Section 3.2. The hardness was measured at 75  $\mu\text{m}$  spacing from the wire substrate interface. This created a linear profile of the hardness with respect to distance from the interface for different ultrasonic currents. The bond current of 440 mA was selected because it was the lowest setting that would achieve bonding of the wire to the substrate. 1500 mA was the highest setting for the machine. 880mA was the optimized value provided by Kulich and Soffa for the specific wire bonder, substrate material, and wire material. The data in Table 6, the hardness at different distances from the interface for wires bonded at

varying ultrasonic currents, is depicted in Figure 29. A more detailed figure with error bars is located in Appendix A, Figure A-1.

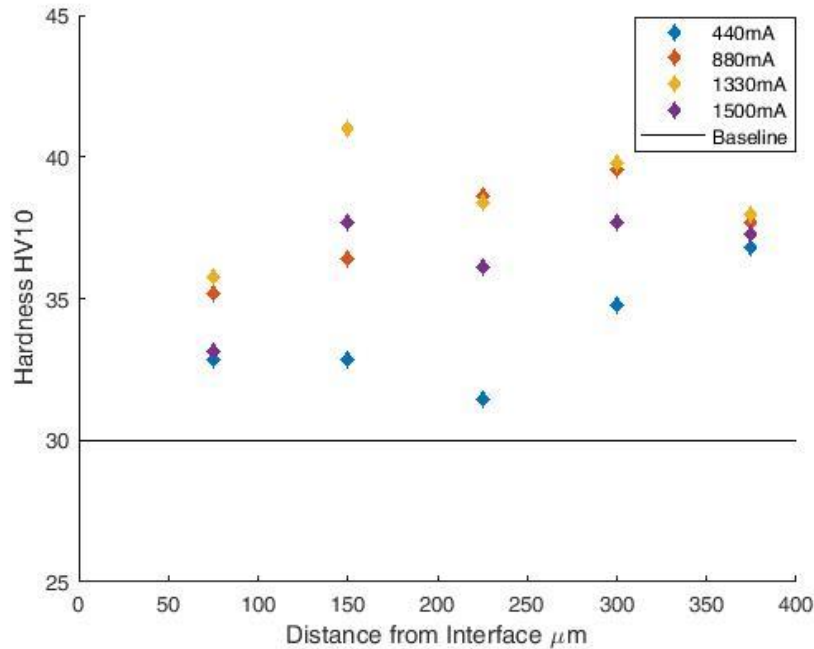


Figure 29- Hardness profiles in bonded wires with different ultrasonic current.

The hardness profiles increase with higher ultrasonic currents until 1500 mA. From 1330 mA to 1500 mA the profiles have an inflection point and the hardness profile decreases. The hardness at 375 μm from the interface is consistent for all bonding currents. The hardness profiles are a result of the interplay between strain hardening and ultrasonic softening. There is a region of high hardness from the plastic deformation at the interfaces, which is adjacent to a region of lower hardness. The area of lower hardness occurs up to 100 μm from the interface. The region of low hardness appears next to the wire-substrate and wire-bond-tool interfaces. Figure 30 illustrates the schematic of the hardness profile in the wire.

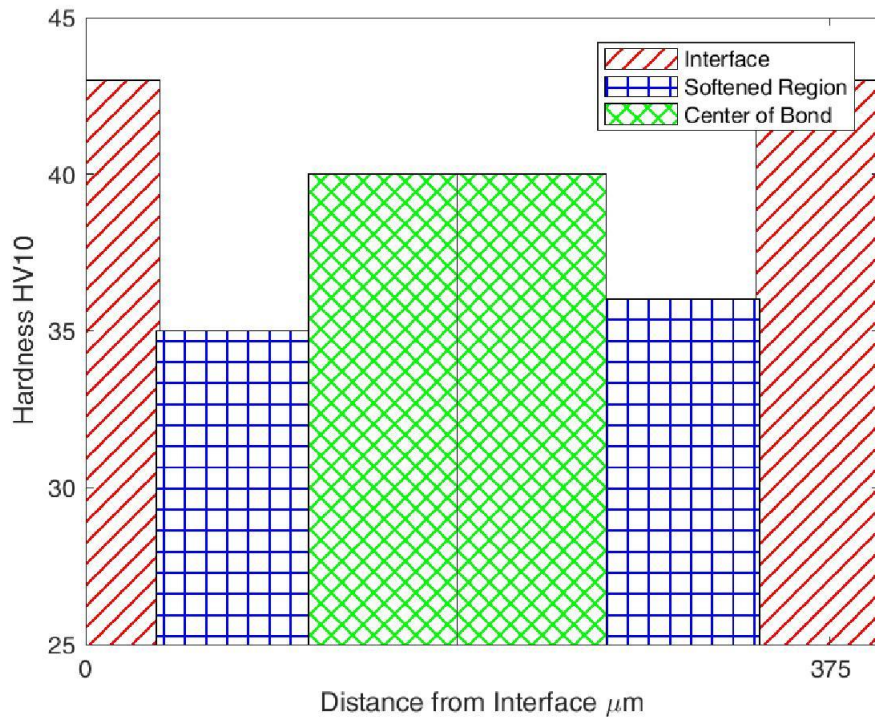


Figure 30- Schematic of Hardness profile.

The reason the softened region appears after the highly deformed interface could be its proximity to the ultrasonic vibration at the interfaces. The vibration would be mostly experienced at these sites. The ultrasonic softening is most extreme at the interfaces, but also results in the largest wire deformation. The dip in hardness, such as in Figure 6, was corroborated by the microhardness data collected in this work [27]. As a result, the plastic deformation is dominant at the interface and becomes less impactful further from the interface. The center of the wire does not see as much of the ultrasonic softening, but it is affected by the global deformation resulting in strain hardening in the wire.

#### 4.2.2 Time Dependence

Table 2 outlined the key bonding parameters. After the effect of bond power was studied, the effect of hold time at specific ultrasonic currents was analyzed. This allowed for more

investigation into the effect of ultrasonic current on the hardness. Changing the duration of time held at a specific ultrasonic current can be used to determine if the effects of ultrasonic vibrations is time dependent. Holding the ultrasonic current constant, the effect of hold time was studied, as shown in Figure 31. The sample was prepared at 880 mA. Appendix B Figure B-1 has error bars added to Figure 31 to show the deviation of the data.

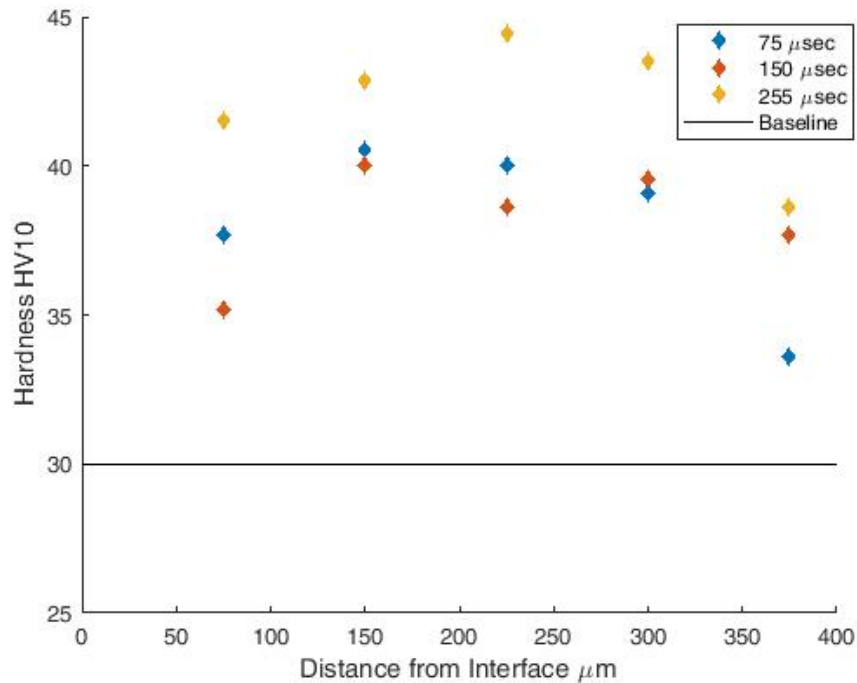


Figure 31- 880mA Ultrasonic Current with different hold times.

The hold time is the amount of time the bonder holds at the steady-state ultrasonic vibration conditions, Figure 14 and Table 2. The hold times studied were 75 μsec, 150 μsec and 255 μsec. A hold time of 150 μsec was standard in this work unless otherwise specified. Reducing the hold time did not alter the resulting hardness profile. This is most likely because the sample was prepared at 880 mA and at this low bond current and lower hold time the transient start power setting was dominate in determining the deformation, Figure 14 and Table 2. The start power

was equivalent to 1000 mA, which is higher than the steady state current. As a result, deformation is mostly a result of the initial 1000 mA starting current instead of a result of holding at the lower steady state bond current. More deformation and a higher hardness profile was achieved by bonding the wire for a longer time. The effect of the larger starting ultrasonic current becomes less as the hold time is increased and the bond spends a longer time under lower steady state bonding current.

The same study of hold time was done at the highest bond current to avoid the starting power effects. Instead of looking at the hardness directly, the deformation was analyzed instead, Figure 32. Only one set of data was collected as a result no statistical analysis was done on the data in Figure 32.

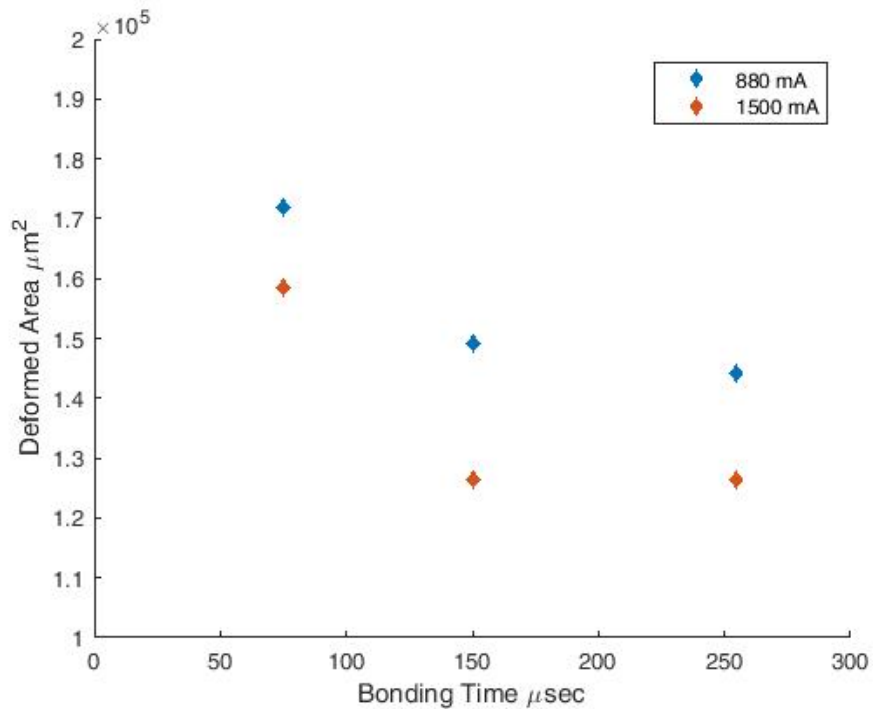


Figure 32- Time dependent deformation.

The highest bond current was selected, 1500 mA, to achieve the highest amount of deformation, and compared to the sample from Figure 31, bonded at 880 mA. At the same bonding time, more deformation is achieved with a higher ultrasonic current. However, when one compares the samples bonded with different conditions but result in the same deformation, the sample with a higher ultrasonic current has a lower hardness. This can be attributed to more ultrasonic vibration reducing the effect of strain hardening. For example, at 75  $\mu$ sec with 1500 mA bond current results in a hardness of 33.9 HV; when this result was compared to the hardness at 150  $\mu$ sec with 880 mA bond current the hardness was 38.2 HV. Their deformed areas are very similar, but the sample with the higher ultrasonic current has a lower hardness. This result suggests that samples with the same amount of deformation, and thus same amount of strain hardening but higher ultrasonic current, result in a lower hardness.

### **4.3 Nano-indentation**

Microindentation is limited in the resolution of the hardness profile that it can measure. In this study, the spacing was limited to 75  $\mu$ m. Using nanoindentation, the spacing was reduced to 15  $\mu$ m. In addition, the smaller indents and the automated testing allowed for more data points to be collected from a single sample. Since the multiple unloading technique was proven to be effective and accurate in Section 3.6, this allowed for multiple data points to be collected at each position. Since more data points were collected, the entire bond was not tested due to time limitations. The testing was focused near the substrate wire interface.

The 3D plots in Figure 33 show the hardness in pascals with varying bond currents. Instead of a linear profile in Figure 29, Figure 33 can show any variation across the wire.

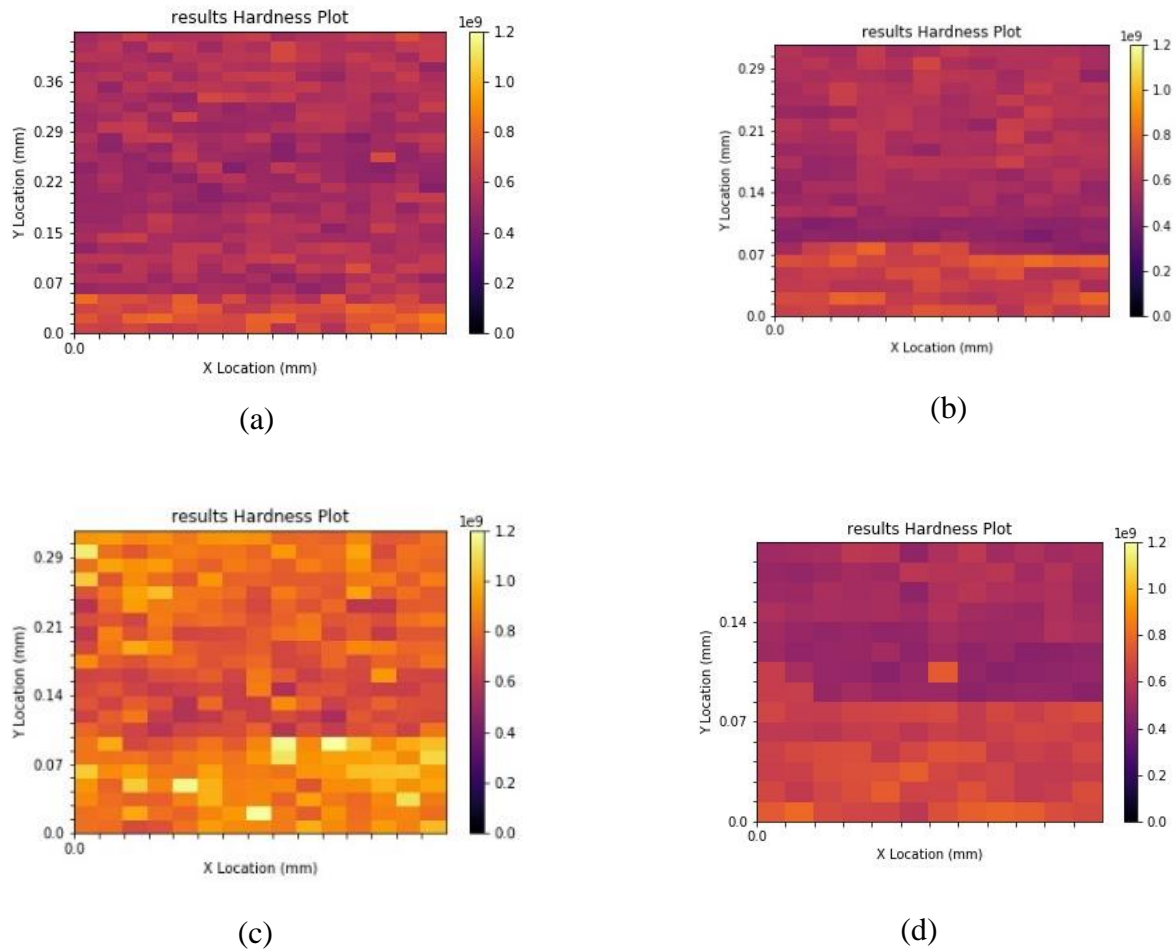


Figure 33- Hardness profiles from nanoindentation (a) 440 mA (b) 880 mA (c) 1330 mA (d) 1500 mA.

The samples tested were the same samples used in the microindentation testing, but a different bond analyzed. Each sample was prepared with multiple bonds for testing. This limited the variability from substrate and wire differences.

The nanoindentation data in Figure 34 confirmed the results from microindentation tests, Figure 29. Appendix C, Figure C-1, contains Figure 34 with the addition of error bars to show the deviation of the data collected. The data used to generate the 3D plots was averaged at each distance from the interface. This generated a linear plot created from the microhardness data (Figure 29).

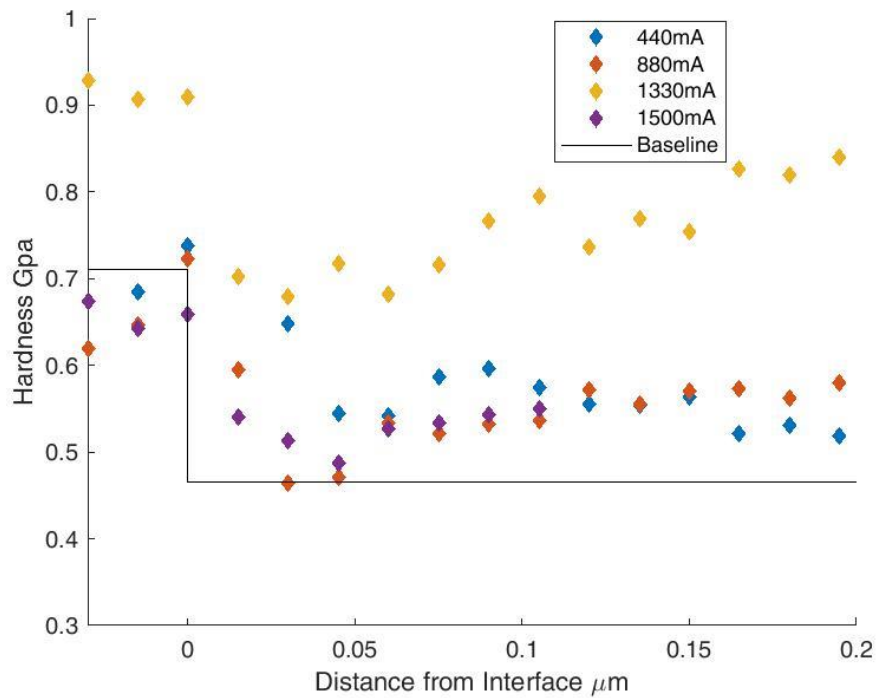


Figure 34- Nanoindentation hardness profile.

The hardness had the same profile as depicted in Figure 29. The hardness profile was maximal at 1330 mA and this result held true for nanoindentation. The 1500 mA had a lower hardness profile than the 1330 mA sample. The data shows consistent results from both the microindentation, as well as, the nanoindentation test method. There was not a measurable increase in the hardness for the 440 mA samples to the 1330 mA samples as in the microindentation data, despite this inconsistency the hardness profile depicted in Figure 30 was validated.

## **5 Conclusion**

### **5.1 Summary and Conclusions**

The effect of ultrasonic wire bonding on mechanical properties was studied by performing microhardness and nanoindentation tests. A program was created that processed microscope pictures of Vickers hardness measurements and calculated the microhardness. It was determined that applying ultrasonic vibration reduces the strain hardening caused by the plastic deformation induced during the bonding process. A profile was measured within the bonds as a function of distance from the substrate interface. An area of low hardness was measured 50-75  $\mu\text{m}$  from the substrate and bond tool interfaces. The effect of increased bond power was determined to have an increased hardness up to 1330 mA bond current. Currents higher than 1330 mA resulted in lower hardness. Bonding hold time was also investigated and found to increase the amount of deformation as well as result in a higher hardness. Nanoindentation corroborated the microhardness tests and proved to be a viable test method.

### **5.2 Future Work**

Future studies would focus on understanding the effect of other bonding parameters on mechanical properties. This research created and analyzed tools that could be used for future studies. Future studies could examine the effect of hold time or normal force as well as investigate the change in mechanical properties to the substrate. The research presented was limited to investigating the properties in the wire. In addition, wires with the same amount of plastic deformation could be made with different ultrasonic powers by varying hold time, normal force, or other bonding parameters to study the interplay of ultrasonic softening and strain hardening.

## 6 References

- [1] M. Schneider-Ramelow, U. Geibler, S. Schmitz, W. Gruble and S. Schuch, "Development and Status of Cu Ball/Wedge Bonding in 2012," *Journal of electronic materials*, vol. 42, no. 3, pp. 558-595, 2013.
- [2] P. Chauhan, A. Choubey, Z. Zhong and M. Pecht, *Copper Wire Bonding*, New York: Springer, 2014.
- [3] Y. Long, J. Twiefel and J. Wallaschek, "A review on the mechanisms of ultrasonic wedge-wedge bonding," *Journal of Materials Processing Technology*, vol. 245, pp. 241-258, 2017.
- [4] O. Anderson, H. Christensen and P. Andreatch, "Technique for Connecting Electrical Leads to Semiconductors," *Journal of Applied Physics*, vol. 28, p. 923, 1957.
- [5] J. Devine, "Joining Metals with Ultrasonic," *Machine Design*, vol. 56, pp. 91-95, 1984.
- [6] B. Langenecker, "Effects of Ultrasound on Deformation Characteristics," *IEEE Transactions on Sonics and Ultrasonics*, vol. 13, no. 1, pp. 1-8, 1966.
- [7] P. Uthe, "Variables affecting weld quality in ultrasonic Al wire bonding," *Solid State technol*, vol. 5, pp. 72-77, 1969.
- [8] H. Krye, "Melting Phenomena in Solid-state Welding Processes," *Welding Journal*, vol. 56, pp. 154-158, 1977.
- [9] J. Krzanowski, "A Transmission Electron Microscopy Study of Ultrasonic Wire Bonding," *IEEE Transactions on Components, Hybrids, and Manufacturing Technology*, vol. 13, no. 1, pp. 176-181, 1990.
- [10] H. Daniels, "Ultrasonic Welding," *Ultrasonics*, vol. 3, no. 4, pp. 190-196, 1965.
- [11] K. Chen, Y. Zhang and H. Wand, "Effect of acoustic softening on the thermal-mechanical process of Ultrasonic Welding," *Ultrasonics*, vol. 75, pp. 9-21, 2017.
- [12] R. Pohlman and E. Lehfeltdt, "Influence of ultrasonic vibration on metallic friction," *Ultrasonics*, vol. 4, no. 4, pp. 178-185, 1966.
- [13] J. Hung and C. Lin, "Investigations on the material property changes of ultrasonic-vibration assisted aluminum alloy upsetting," *Materials & Design*, vol. 45, pp. 412-420, 2013.
- [14] S. Bagherzadeh and K. Abrinia, "Effect of Ultrasonic Vibration on Compression Behavior and Microstructural Characteristics of Commercially Pure Aluminum," *Journal of Materials Engineering and Performance*, vol. 24, no. 11, pp. 4364-4376, 2015.

- [15] F. Osterwald, *Verbindungsbildung beim ultraschall-Drahtbenden: Einflußder Schwingungsparameter und Modellvorstellungen (Doctoral dissertation)*, Technical University of Berlin (in German), 1999.
- [16] C. Breach and F. Wulff, "A brief review of selected aspects of the materials science of ball bonding," *Microelectronics Reliability*, vol. 50, no. 1, pp. 1-20, 2010.
- [17] A. Shah, H. Gaul, M. Schneider-Ramelow, H. Reichl, M. Mayer and Y. Zhou, "ultrasonic friction power during Al wire wedge-wedge bonding," *Journal of Applied Physics*, vol. 106, pp. 013503-1-013503-8, 2009.
- [18] M. Sheaffer and L. Levine, "How to Optimize and Control the Wire Bonding Process: Part I," *Solid State Technology*, vol. 33, pp. 119-123, 1990.
- [19] E. Arjmand, P. Agyakwa and C. Johnson, "Reliability of thick Al wire: a Study of the effects of wire bonding parameters on thermal cycling degradation rate using non-destructive methods.," *Microelectronics Reliability*, vol. 54, no. 9-10, pp. 2006-20012, 2014.
- [20] Y. Tian, C. Wang, I. Lum, M. Mayer, J. Jung and Y. Zhou, "Investigation of ultrasonic copper wire wedge bonding on Au/Ni plated Cu substrates at ambient temperature," *Journal of Materials Processing Technology*, vol. 208, no. 1-3, pp. 179-186, 2008.
- [21] W. Fu-Liang, L. Jun-hui, H. Lei and Z. Jue, "Effect of ultrasonic power on bonding strength and interface microstructure," *Transactions of Nonferrous Metals Socieity of China*, vol. 17, pp. 606-611, 2007.
- [22] W. Fu-liang, H. Lei and Z. Jue, "Study of Ultrasonic Power Paramert on the Large Aluminum Wire Wedge Bonding Strength," *High Density Microsystem Design and Packaging and Component Failure Analysis*, pp. 1-4, 2005.
- [23] C. Kaestle and J. Franke, "Comparative analysis of the process window of aluminum and copper wire bonding for power electronics applications," *014 International Conference on Electronics Packaging (ICEP)*, pp. 335-340, 2014.
- [24] A. Rollet and U. F. Kocks, "A review of the stages of work hardening," *Solid State Phenomena*, vol. 35, pp. 1-18, 1994.
- [25] U. Kocks and H. Mecking, "Physics and phenomology of strain hardening: the FCC case," *Progresss in Materials Science*, vol. 48, pp. 171-273, 2003.
- [26] J. Kreyca and E. Kozeschnik, "Flow Stress Modeling and Microstructure Development during Deformation of Metallic Materials," *Materials Science Forum*, vol. 892, pp. 44-49, 2016.

- [27] M. Broll, U. Geissler, J. Höfer, S. Schmitz, O. Wittler and K. Lang, "Microstructural evolution of ultrasonic-bonded aluminum wires," *Microelectronics Reliability*, vol. 55, pp. 961-968, 2015.
- [28] Z. Yao, G. Kim, Z. Wang, L. Faidley, Q. Zou, D. Mei and Z. Chen, "Acoustic softening and residual hardening in aluminum: Modeling and experiments," *International Journal of Plasticity*, vol. 39, pp. 75-87, 2012.
- [29] Y. Zhou, *Microjoining and Nanojoining*, Cambridge: Woodhead Publishing/CRC Press, 2008.
- [30] H. Seppanen, R. Kurppa, A. Merilainen and E. Haeggstrom, "Real Time Contact Resistance Measurement to Determine When Microwelds Start to Form During Ultrasonic Wire Bonding," *Microelectronic Engineering*, vol. 104, pp. 114-119, 2013.
- [31] H. Gaul, A. Shah, M. Mayer, Z. Zhou, M. Schneider-Ramelow and H. Reichl, "The ultrasonic wedge/wedge bonding process investigated using in situ real-time amplitudes from laser vibrometer and integrated force sensor," *Microelectronic Engineering*, vol. 87, pp. 537-542, 2010.
- [32] L. Merkle, T. Kaden, M. Sonner, A. Gademann, J. Turki, C. Dresbach and M. Petzold, "Mechanical Fatigue Properties of Heavy Aluminium Wire Bonds for Power Applications," *2nd Electronics System Integration Technology Conference*, vol. 2, pp. 1363-1367, 2008.
- [33] G. Khatibi, B. Weiss, J. Bernardi and S. Schwarz, "Microstructural Investigation of Interfacial Features in Al Wire Bonds," *Journal of Electronic Materials*, vol. 41, no. 12, pp. 3436-3446, 2012.
- [34] N. Murdeshwar and J. Krzanowski, "A microstructural study of dislocation substructures formed in metal foil substrates during ultrasonic wire bonding," *Metallurgical and Materials Transactions A*, vol. 28, no. 12, p. 2663-2671, 1997.
- [35] K. Pederson, D. Benning, P. Kristenesen, V. Popok and K. Pedersen, "Interface structure and strength of ultrasonically wedge bonded heavy aluminium wires in Si-based power modules," *Mater Sci: Mater Electron*, vol. 25, pp. 2863-2871, 2014.
- [36] K. Siu, A. Ngan and I. Jones, "New insight on acoustoplasticity – Ultrasonic irradiation enhances," *International Journal of Plasticity*, vol. 27, pp. 788-800, 2011.
- [37] H. Huang, A. Pequegnat, B. Chang, M. Mayer, D. Du and Y. Zhou, "Influence of superimposed ultrasound on deformability of Cu," *Journal Of Applied Physics*, vol. 106, no. 11, pp. 113514-1-113514-6, 2009.

- [38] W. Oliver and G. Pharr, "An Improved technique for determining hardness and elastic modulus using load displacement sensing indentation experiments," *J. Mater. Res.*, vol. 7, no. 6, pp. 1564-1583, 1992.
- [39] M. Dao, N. Chollacoop, K. Van Vliet, T. Venkatesh and S. Suresh, "Computational Modeling of the Forward and Reverse Problems in Instrumented Sharp Indentation," *Acta Materialia*, vol. 49, pp. 3899- 3918, 2001.
- [40] N. Ogasawara, N. Chiba and X. Chen, "Measuring the plastic properties of bulk materials by single indentation test," *Scripta Materialia*, vol. 54, pp. 65-70, 2006.
- [41] G. Pharr and A. Bolshakov, "Understanding Nanoindentation unloading curves," *J. Mater. Res.*, vol. 17, no. 10, pp. 2660-2671, 2002.
- [42] G. M. Pharr and A. Bolshakov, "Influences of pileup on the measurement of mechanical properties by load and depth sensing indentation techniques," *J. Mat Res.*, vol. 13, no. 4, pp. 1049-1058, 1998.
- [43] J. Wang, P. Hodgson and C. Yang, "Effects of mechanical properties on the contact profile in Berkovich nanoindentation of elastoplastic materials," *J. Mater. Res.*, vol. 27, no. 1, pp. 313-319, 2012.
- [44] S. M. Walley, "Historical origins of indentation hardness," *Materials Science and Technology*, vol. 28, no. 9, pp. 1028-1148, 2012.
- [45] E. A. Jr. and G. Murphy, "Correlation of Vickers hardness number, modulus of elasticity, and the yield strength for ductile metals," *United States Atomic Energy Commission*, 1953.
- [46] E. Pavlina and C. V. Tyne, "Correlation of Yield Strength and Tensile Strength with Hardness for Steels," *Journal of Materials Engineering and Performance*, vol. 17, no. 6, pp. 888-893, 2008.
- [47] D. Tabor, "The Hardness and Strength of Metals," *Journal Institute of Metals*, vol. 79, pp. 1-18, 1951.
- [48] J.R.Cahoon, W. H. Broughton and A. R. Kutzak, "The Determination of Yield Strength From Hardness Measurements," *Metallurgical Transactions*, vol. 2, no. 7, pp. 1973-1978, 1971.
- [49] C. Dresbach, M. Mittag, M. Petzold, E. Milke and T. Müller, "Mechanical Properties and Microstructure of Heavy Aluminum Bonding Wires for Power Applications," *European Microelectronics and Packaging Conference*, pp. 1-8, 2009.

- [50] R. L. Smith and G. E. Sandland, "An Accurate Method of Determining the Hardness of Metals, with Particular Reference to Those of a High Degree of Hardness," *Proceedings - Institution of Mechanical Engineers*, vol. 1, pp. 623-643, 1922.
- [51] "Standard Test Methods for Vickers Hardness and Knoop Hardness of Metallic Materials," *ASTM*, pp. 1-27, 2018.
- [52] P. P. Filho, T. Cavalcante, V. H. de Albuquerque and J. M. Tavares, "Brinell and Vickers Hardness Measurements Using Image Processing And Analysis Techniques," *Journal of Testing and Evaluation*, vol. 38, no. 1, pp. 88-94, 2010.
- [53] K. Suganeswaran, N.Nithyavathy, R.Parameshwaran, G.Raja and M. Prakash, "Hardness Measurement using Image Analysis in Matlab," *International Journal of Latest Trends in Engineering and Technology*, vol. 5, no. 4, pp. 288-297, 2015.
- [54] F. O. Sonmez and A. Demir, "Analytical relations between hardness and strain for cold formed parts," *Journal of Materials Processing Technology*, vol. 186, no. 1-3, pp. 163-173, 2007.
- [55] Image Processing Toolbox: User's Guide, Mathworks, 2016.
- [56] M. Gadermayr, "Vickers Image Segmentation Using Active Contours," *University of Salzburg*, 2012.
- [57] Hysitron, TI Premier User Manual, Vol. 9.4.0914.
- [58] H. J. Kleemola and M. Nieminen, "On the Strain-Hardening Parameters of Metals," *Metallurgical Transactions*, vol. 5, no. 8, pp. 1863-1866, 1974.
- [59] I. Lum, M. Mayer and Y. Zhou, "Footprint Study of Ultrasonic Wedge-Bonding with Aluminum wire on Copper Substrate," *Journal of Electronic Materials*, vol. 35, no. 3, pp. 433-442, 2006.
- [60] W. S. Loh, M. Corfield, H. Lu, S. Hogg, T. Tilford and C. M. Johnson, "Wire Bond Reliability for power Electronic Modules-Effect of Bonding Temperature," *International Conference on Thermal, Mechanical and Multi-Physics Simulation Experiments in Microelectronics and Micro-Systems*, pp. 1-6, 2007.
- [61] F. Ahmadi, M. Farzin, M. Meratian, S. M. Loeian and M. R. Forouzan, "Improvement of ECAP process by imposing ultrasonic vibrations," *Int J Adv Manuf Technol*, vol. 79, pp. 503-512, 2015.
- [62] J. Yeung and L. Keong, "Hardness Measurement of Copper Bonding Wire," *Procedia Engineering*, vol. 75, pp. 134-139, 2014.

- [63] H. Zhou, H. Cui, Q. Qin, H. Wang and Y. Shen, "A comparative study of mechanical and microstructural characteristics of aluminium and titanium undergoing ultrasonic assisted compression testing," *Materials Science and Engineering: A*, vol. 682, no. 13, pp. 376-388, 2017.
- [64] Y. Chan, J. Kim, D. Liu, P. Liu, Y. Cheung and M. Ng, "Effects of Bonding frequency on Au wedge wire bondability," *Journal of Materials Science: Materials in Electronics*, vol. 19, no. 2, p. 281–288, 2008.
- [65] U. Geibler, M. Schneider-Ramelow and H. Reichl, "Hardening and Softening in AlSi1 Bond Contacts During Ultrasonic Wire Bonding," *IEEE Transactions on Components and Packaging Technologies*, vol. 32, no. 4, pp. 794-799, 2009.
- [66] G. Harman and J. Albers, "The Ultrasonic Welding Mechanism as Applied to Aluminum- and Gold-Wire Bonding in Microelectronics," *IEEE Transactions on Parts, Hybrids, and Packaging*, vol. 13, no. 4, pp. 406-412, 1977.
- [67] I. Lum, C. Hang, M. Mayer and Y. Zhou, "In Situ Studies of the Effect of Ultrasound During Deformation on Residual Hardness of a Metal," *Journal of Electronic Materials*, vol. 38, no. 5, pp. 647-654, 2009.
- [68] W. Fu-Liang, L. Jun-hui, H. Lei and Z. Jue, "Effect of ultrasonic power on wedge bonding strength and interface microstructure," *I'r'ins. Nonferrous Mct. Soc*, vol. 17, pp. 606-611, 2007.
- [69] K. ZENG and C. Chiu, "An analysis of load -penetration curves from instrumented indentation," *Acta Materialia*, vol. 49, no. 17, p. 3539–3551, 2001.

## Appendix A

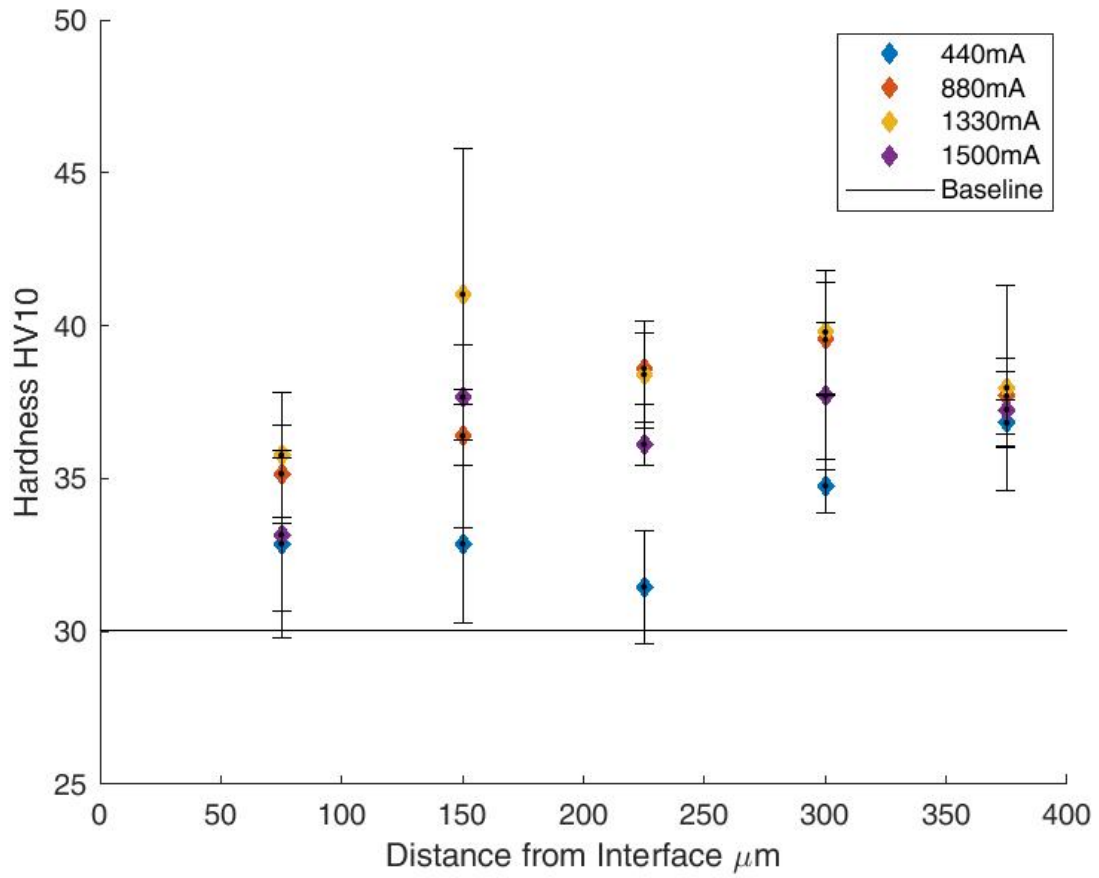


Figure A- 1-Hardness profiles in bonded wires with different ultrasonic current with error bars.

# Appendix B

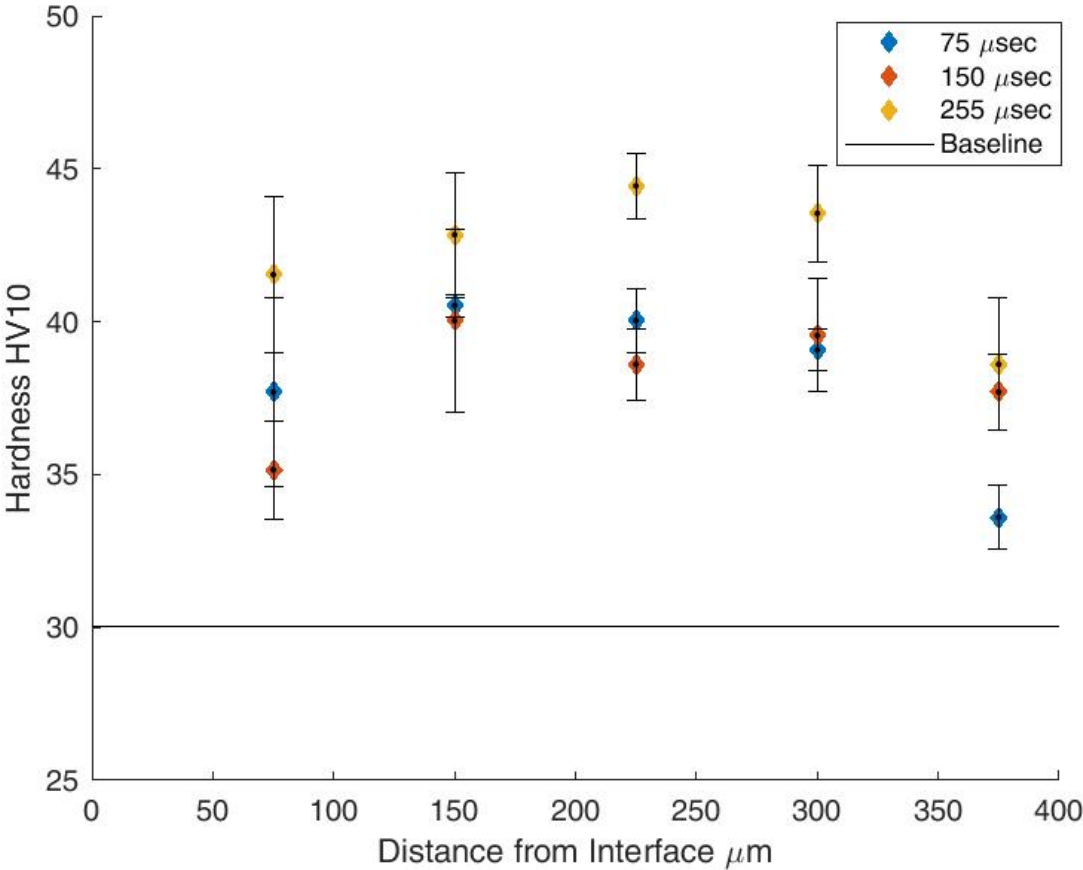


Figure B- 1-880mA Ultrasonic Current with different hold times with error bars.

## Appendix C

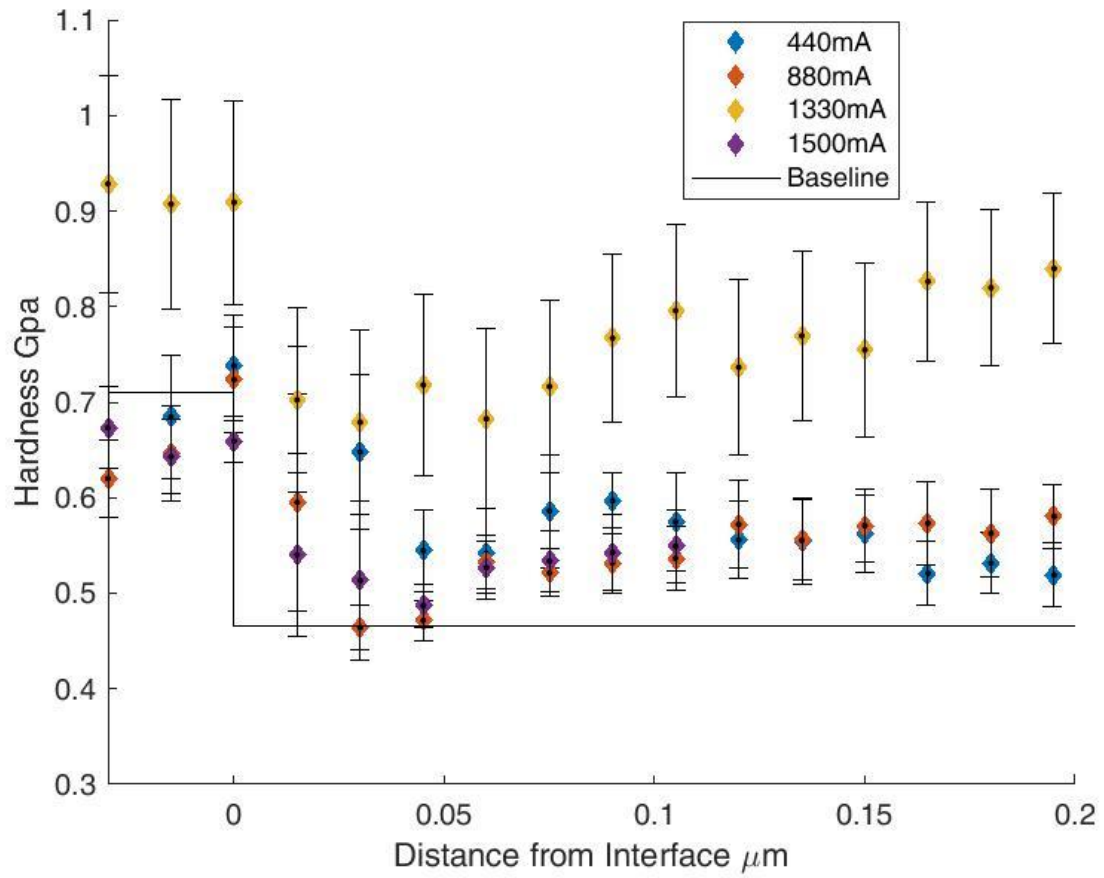


Figure C- 1- Nanoindentation hardness profile with error bars.

## Appendix D

Image Analysis MATLAB script described in Section 3.5.

```
%Matt McKay
%5/21/2017
%Program to measure vickers hardness from an image

%set variables
scalebarleng=.1; %mm
load= .010; %kgf
k=0; %initialize var
f=1;
w=1;
%end set varsi

%read in image/convert to binary
I1=imread('255time\75_255_3_2_25.tif'); %reads in image
I=rgb2gray(I1); %creates grayscale image
grey=graythresh(I); %calculates threshold for use in next line
BW=im2bw(I,grey); %creates bw picture

%end image read in/preprocessing

%calculate length of scale bar
A=edge(I,'canny',grey-0.1); %finds all the boundaries between black and white bodies
cc = bwconncomp(A); %finds connected bodies
measurements = regionprops(A); %find properties of connected bodies, ie area etc.

for k = 1 : length(measurements) %loops through bodies seraching for long thin feature which is
defining characteristic of scale bar
    thisBB = measurements(k).BoundingBox;
    if thisBB(3) >= 200 && thisBB(4)>=3 &&thisBB(4)<=6 %scale bar criteria
        scalebarindex=k; %saves index of what body was the scale bar
        scalebarpixels=thisBB(3); %saves length of scale bar in pixels
    end
end
%end scalebarlegnth calc
;scalebarpixels=381;
%filter picture

BW1=bwareaopen(not(BW),600,8); %removes small black bodies
BW1=bwareaopen(BW1,1000,4); %removes small white bodies

%end filtering

%Calculate hardness
stats=regionprops(BW1); % get properties of BW bodies
```

```

arindex=zeros( length(stats),1); %intialize var
indentar=zeros(length(stats),1); %intialize var

%for loop that checks to see if body is an indent based on "squareness" and
%size
for h = 1 : length(stats)
    thisBw = stats(h).BoundingBox;
    q=thisBw(3)/thisBw(4);
    if (thisBw(3)/thisBw(4))>=.875 && (thisBw(3)/thisBw(4))<=1.125
    &&stats(h).BoundingBox(3)*stats(h).BoundingBox(4)>400
        arindex(f,1)=h;
        indentar(f,1)=stats(h).BoundingBox(3)*stats(h).BoundingBox(4);
        f=f+1;
    end

end
hardness=zeros(f-1,3); %intialize var
conver=scalebarleng/scalebarpixels; %conversion ration from pixels to mm

%hardness(1,1)=0; %sets top left indent at (0,0) fot plot
%hardness(1,2)=0;

%calculates hardness for each indent and sets location for plot
for w=1 : f-1
    davg=((stats(arindex(w)).BoundingBox(3))*conver+(stats(arindex(w)).BoundingBox(4))*conver)/2;
    %average diagonals from bounding box sides, converted from pixel to mm
    hardness(w,3)=(1.8544*load)/davg^2; %compute vickers hardness
    hardness(w,1)= conver*stats(arindex(w)).Centroid(1); %set x pos
    hardness(w,2)= conver*stats(arindex(w)).Centroid(2) ; %set y pos
end
%hardness(1,1)=0;
%hardness(1,2)=0;
% end calculate harndess

% outputs

%display indents
imshow(BW1);
for y=1: f-1

rectangle('Position', stats(arindex(y)).BoundingBox, 'EdgeColor', 'red', 'LineWidth',2.5);
hold
end
%end diplay

% graph hardness results
xlin = linspace(min(hardness(:,1)),max(hardness(:,1)),h); %creates uniform lin in x
ylin = linspace(min(hardness(:,2)),max(hardness(:,2)),h); %creates uniform line in y
[X,Y] = meshgrid(xlin,ylin); %creats uniform grid from not uniform data
f = scatteredInterpolant(hardness(:,1),hardness(:,2),hardness(:,3)); %interpolate non unitorm data to
uniform grida

```

```
Z = f(X,Y);  
figure(); %new figure  
contourf(X,Y,Z, 0:2:50); %plot hardness results  
caxis([0, 50])  
colorbar %creates uniform color bar for all graphs so a comparison can be made  
% end graphing  
  
%end outputs
```

## Appendix E

The code below was used to process the process the nanoindentation data. The code is written in Python and was run using Python 3.6.

```
# -*- coding: utf-8 -*-
"""
Created on Tue Jul 18 17:50:43 2017
@author: Jamie
"""

#import math as math
#import plotly as pl
import numpy as np          #Imports the necessary libraries
np.set_printoptions(threshold=np.nan)
import matplotlib.pyplot as plt
import sympy as sp
import sys
from astropy.table import Table, Column
#import pandas as pd
import xlswriter
import peakutils

fileDirectory = r"C:\Users\matm\Downloads\S055_1 Wire1-20180308T212031Z-001\S055_1 Wire1"
#Asks for input of the base file directory where the indentation data is located (ex. E:\Lab\S023_8 Closer
MultiUnloading\

txtfile = "\\S055_Wire1_Analysis.txt"          #Asks for input of the indentation summary data file (ex.
S023_CloserMultiUnloading_Analysis.txt)

multiloadtxtfile = "\\S055_Wire1_" #Asks for input of the base for the summary data for each indentation
(ex. S023_CloserMultiUnloading_). Will add correct number endings.

PHDataFile = "\\S055_Wire1_"          #Asks for input of the base for the indentation P-H data
file (ex. S023_CloserMultiUnloading_). Will add correct number endings.

skipNumber = 0

skipRows = np.zeros((1,int(skipNumber)))          #Asks for the indent numbers
that could not be processed correctly and must be skipped/accounted for
```

```

for v in range(0,int(skipNumber)):
    x = 0
    skipRows[0,v] = int(x)

filebase = "results"          #Asks for input of the base filename to save results to (ex.
S023_CloserMultiUnloading_Python). Will add _Results, _nPlot, etc. and save

numPeaks = 14                 #Asks for the number of peaks (unloading intervals) in order to
correctly identify them

overviewFile= np.loadtxt(fileDirectory+txtfile, skiprows=1+2, usecols=range(1,15), delimiter="\t")
#loads the indentation summary data

rows = overviewFile.shape[0] + int(skipNumber)          #Finds the number of indentations by
taking the number of rows in the summary data

xCoord = overviewFile[:,11]-overviewFile[0,11]        #Finds the x and y coordinates of each indentation
relative to the first indentation

yCoord = overviewFile[:,12]-overviewFile[0,12]

s = np.zeros((numPeaks,1))    #Creates the proper size matrices to store properties in later + other basic
setup

n = np.zeros((rows,numPeaks))

E = np.zeros((rows,numPeaks))

YS = np.zeros((rows,numPeaks))

work = np.zeros((rows,numPeaks))

numZero = '0'

ending = '.txt'

Htotal = [];

v = 0.07                    #Poisson's ratio for the indenter tip

Ei = 1140*10**9             #Modulus of Elasticity of the indenter tip

vx = .33                    #Poisson's ratio for 5052-O Aluminum

sys.setrecursionlimit(500)  #Sets the recursion limit for the np.solve numerical solving function

np.set_printoptions(threshold=np.nan) #Disables summary printing

z = sp.Symbol('z')         #Sets symbols for use in numerically solving Ogasawara's eqns
y = sp.Symbol('y')

```

```

w = sp.Symbol('w')
q = sp.Symbol('q')

for v in range(0,int(skipNumber)):    #Fills in missing coordinates for skipped rows
    xCoord = np.insert(xCoord,int(skipRows[0,v]),np.array((2*xCoord[int(skipRows[0,v])-1]-
xCoord[int(skipRows[0,v])-1])),0)
    yCoord = np.insert(yCoord,int(skipRows[0,v]),np.array((yCoord[int(skipRows[0,v])-1])),0)

for num in range(0,rows):    #Repeats for every indentation
    if num in skipRows:    #Adds in zeros if it's a skipped indentation
        work[num] = 0

        zeroMatrix = np.zeros((1,int(numPeaks)))    #Defined a zero matrix to sub in for skipped rows
        if num==0:    #Adds H to Htotal for future use
            Htotal = zeroMatrix
        else:
            Htotal = np.vstack((Htotal,zeroMatrix))

    else:    #If it's not a skipped indentation
        number = str(num)

        if num<10:    #Sets 5 digit number for the ending of the indentation (00000, 00001, etc)
            number = numZero + numZero + numZero + numZero + number
        elif num<100:
            number = numZero + numZero + numZero + number
        elif num<1000:
            number = numZero + numZero + number
        elif num<10000:
            number = numZero + number
        else:
            number = number

```

```

    multiloadData = np.loadtxt(fileDirectory+multiloadtxtfile+number+' LC.txt', skiprows=1+2,
    usecols=range(1,15), delimiter="\t")    #Loads the summary data for that indent

    Er = multiloadData[:,6]*10**9          #Pulls data from the summary data and converts to base SI
    units

    hc = multiloadData[:,0]*10**9          #Er is the reduced modulus, hc is the max contact depth, C is
    the power fit coefficient,

    C = multiloadData[:,8]                #S is the stiffness, m is the power fit exponenet, hf is the power fit
    offset, heff is the max depth (not

    S = multiloadData[:,2]*10**3          #accounting for pitting), and H is the hardness

    m = multiloadData[:,10]

    hf = multiloadData[:,9]*10**9

    heff = multiloadData[:,5]*10**9

    H = multiloadData[:,7]*10**9

    if num==0:                            #Adds H to Htotal for future use

        Htotal = H

    else:

        Htotal = np.vstack((Htotal,H))

    depth = np.loadtxt(fileDirectory+PHDataFile+number+ending, skiprows=0+1+2+3, usecols=[0],
    delimiter="\t")*10**9    #Loads depth and load data from the P-H data for that indent

    load = np.loadtxt(fileDirectory+PHDataFile+number+ending, skiprows=0+1+2+3, usecols=[1],
    delimiter="\t")*10**6

    distanceApart = 200                    #Sets starting distance between local
    maxima (to be used in isolating each unloading cycle)

    locs = peakutils.peak.indexes(load, thres = .1, min_dist = distanceApart)    #Finds local maximas
    at least 200 apart

    while locs.shape[0] != numPeaks:      #Checks whether that yielded the
    right number of peaks and if not adjusts the distance apart until the correct number are found

        if locs.shape[0] > numPeaks:

            distanceApart = distanceApart + 1

        elif locs.shape[0] < numPeaks:

            distanceApart = distanceApart - 1

```

```

locs = peakutils.peak.indexes(load, thres = .1, min_dist = distanceApart)

for i in range(0,numPeaks):          #For each peak, calculates the work done during
loading by taking the area under the P-H curve up to that peak

    shortenedDepth = depth[1:locs[i]]
    shortenedLoad = load[1:locs[i]]
    work[num, i] = np.trapz(shortenedLoad,shortenedDepth)

for x in range(0,numPeaks):          #For each peak, calculates properties
                                     #Assigns variables for easy use
    hc[x] = hc[x]
    Er[x] = Er[x]
    C[x] = C[x]
    m[x] = m[x]
    S[x] = S[x]
    hf[x] = hf[x]
    heff[x] = heff[x]

    try: #Calculates s (try, except makes it so that if s cannot be calculates, a 0 is substituted instead
of an error being thrown). Saves to temp 1D array
        s[x] = sp.nsolve((-20821*(sp.log(Erx/z))**3.0 + 2.6502*(sp.log(Erx/z))**2.0 -
3.7040*(sp.log(Erx/z)) + 2.7725) - (work[num,x]/(hc**3.0*z)), z, 10**8)
    except:
        s[x] = 0#float('NaN')

    try: #Calculates n and saves it to a matrix where each row is an indent and each column is a
partial unloading
        n[num,x] = np.array(sp.nsolve(((-.04783*y**2+.04667*y-
.01906)*(sp.log(Erx/float(s[x])))**3.0 + (.6455*y**2-.6325*y+.2239)*(sp.log(Erx/float(s[x])))**2.0 + (-
2.298*y**2+2.025*y-.4512)*(sp.log(Erx/float(s[x]))) + (2.050*y**2-1.502*y+2.109)) -
Sx/(2.0*hc*Erx), y, .2), dtype = float)
    except:
        n[num,x] = 0#float('NaN')

    try: #Same for E

```

```

    E[num,x] = sp.solve((((1-v**2)/Ei + (1-vx**2)/w)**-1) - Er[x], w, 10**11)
except:
    E[num,x] = 0#float('NaN')

try: #Same for YS
    YS[num,x] = sp.solve(q*(1+float(E[num,x])*0.0115/q)**float(n[num,x]) - float(s[x]), q,
10**6)
except:
    YS[num,x] = 0#float('NaN')

nNoSkipRows = n          #Removes the skipped row data from each matrix (used in taking averages,
etc)
ENoSkipRows = E
YSNoSkipRows = YS
if skipNumber != 0:
    print('nonzero')
    for num in range(0,int(skipNumber)):
        print(num)
        nNoSkipRows = np.delete(nNoSkipRows, skipRows[0,num], axis = 0)
        ENoSkipRows = np.delete(ENoSkipRows, skipRows[0,num], axis = 0)
        YSNoSkipRows = np.delete(YSNoSkipRows, skipRows[0,num], axis = 0)

ave_n = np.mean(nNoSkipRows, axis=0)          #Takes average n at each
partial unloading (not including the skipped rows)
ave_E = np.mean(ENoSkipRows, axis=0)          #Same for E and YS
ave_YS = np.mean(YSNoSkipRows, axis=0)

Load = np.array(range(numPeaks))+1            #Creates an array of numbers 1,
2, ... , number of partial unloadings

results = Table([Load, ave_E, ave_n, ave_YS], names=('Load', 'ave_E', 'ave_n', 'ave_YS')) #Makes a
table of the average data

results.add_row((999, np.mean(E), np.mean(n), np.mean(YS)))          #Adds a row to
absolute averages over all indentations and all partial unloads

name = fileDirectory + filebase + '_Results.xlsx'    #Creates the excel file name

```

```

workbook = xlswriter.Workbook(name)           #Makes the excel file
worksheet1 = workbook.add_worksheet('Sheet1') #Adds the first excel sheet
worksheet1.write(0, 0, 'Load')                #Labels the columns
worksheet1.write(0, 1, 'ave_E')
worksheet1.write(0, 2, 'ave_n')
worksheet1.write(0, 3, 'ave_YS')

row = 1                                       #Sets data start point (0,1)
col = 0

nSave = n                                     #Saves copies of each property matrix b/c writing to excel tends to
overwrite them with a single value
ESave = E
YSSave = YS
LoadSave = Load
for Load, ave_E, ave_n, ave_YS in results:    #Writes each piece of data
    worksheet1.write(row, col, Load)
    worksheet1.write(row, col + 1, ave_E)
    worksheet1.write(row, col + 2, ave_n)
    worksheet1.write(row, col + 3, ave_YS)
    row += 1
worksheet1.write((row-1), 0, 'AVG')          #Changes the label for the averages to avg instead of 999

E = ESave                                   #Reset properties
Load = LoadSave

worksheet2 = workbook.add_worksheet('Sheet2') #Adds the second excel sheet
for row, data in enumerate(Load):           #Writes the load numbers as the column headings
    worksheet2.write_row(0, 0, Load)
for t in range(0,E.shape[0]):
    for row, data in enumerate(E[t,:]):     #Writes the E data
        worksheet2.write_row(t+1, 0, E[t])

```

```

worksheet2 = workbook.add_worksheet('Sheet3') #Same process for n in sheet 3
for row, data in enumerate(Load):
    worksheet2.write_row(0, 0, Load)
for t in range(0,n.shape[0]):
    for row, data in enumerate(n[t,:]):
        worksheet2.write_row(t+1, 0, n[t])

worksheet2 = workbook.add_worksheet('Sheet4') #Same process again for yield strength in sheet 4
for row, data in enumerate(Load):
    worksheet2.write_row(0, 0, Load)
for t in range(0,YS.shape[0]):
    for row, data in enumerate(YS[t,:]):
        worksheet2.write_row(t+1, 0, YS[t])

workbook.close() #Closes and saves the excel sheet

xCoordList = list(xCoord) #Makes the coordinate data into lists and then counts the
dimensions and reshapes the x and y data to get an (x,y) grid
yCoordList = list(yCoord)
xDim = xCoordList.count(xCoord[1])
yDim = yCoordList.count(yCoord[1])
xCoord2D = xCoord.reshape((xDim, yDim))
xCoord2D = np.append(xCoord2D, np.full((xDim,1),(xCoord[yDim-1]+xCoord[1])), 1) #Adds
buffer rows onto the coordinate matrices so all the data shows on the plot
xCoord2D = np.append(xCoord2D, np.reshape(xCoord2D[(xDim-1),:], (1,(yDim+1))), 0)
yCoord2D = yCoord.reshape((xDim, yDim))
yCoord2D = np.append(yCoord2D, np.full((xDim,1),yCoord[yDim-1]), 1)
if xDim > 1:
    yCoord2D = np.append(yCoord2D, np.full((1,(yDim+1)),(yCoord.max()+yCoord2D[1,0])), 0)
else:
    yCoord2D = np.append(yCoord2D, np.full((1,(yDim+1)),1), 0)

```

```

plt.clf()                                #Clears the plot
HIndentAverage = np.mean(Htotal, axis=1)  #Takes the average H at each indent cite
H2D = HIndentAverage.reshape(( xDim, yDim)) #Reshapes the H data to fit the (x,y) grid
for num1 in range(H2D.shape[0]):          #Sets any 'outlying' data points to the mean. This makes the
remaining data easier to look at because more color variation shows
    for num2 in range(H2D.shape[1]):
        if H2D[num1,num2] < np.mean(H2D)/1.5 or H2D[num1,num2] > np.mean(H2D)*1.5:
            H2D[num1,num2] = np.mean(H2D)

plt.pcolor(H2D, cmap = 'inferno')         #Creates a color plot of the H data
plt.title(filebase + ' Hardness Plot')    #Adds a title and axes
plt.xlabel('X Location (mm)')
plt.ylabel('Y Location (mm)')
my_xticks = []                            #Sets the x axes to mark every 20 mm in the x and every 5 mm in the
y
for num in range(0,H2D.shape[1]):
    if num in [0,20,40,60,80,100]:
        my_xticks = np.append(my_xticks,round(float(num*(xCoord.max()-
xCoord.min())/H2D.shape[1]),2))
    else:
        my_xticks = np.append(my_xticks,")
plt.xticks(range(0, H2D.shape[1]), my_xticks)
my_yticks = []
for num in range(0,H2D.shape[0]):
    if num in [0,5,10,15,20,25,30,35,40,45,50,55,60,65,70,75,80,85,90,95,100]:
        my_yticks = np.append(my_yticks,round(float(num*(yCoord.max()-
yCoord.min())/H2D.shape[0]),2))
    else:
        my_yticks = np.append(my_yticks,")
plt.yticks(range(0, H2D.shape[0]), my_yticks)

plt.colorbar()                            #Adds the colorbar for reference

```

```

plt.clim(0, 1200000000)

plt.savefig(fileDirectory + filebase + '_HPlot2.jpg')          #Saves the plot

plt.clf()                #Does the same thing for n, then YS, then H
nIndentAverage = np.mean(nSave, axis=1)
n2D = nIndentAverage.reshape((xDim, yDim))
for num1 in range(n2D.shape[0]):
    for num2 in range(n2D.shape[1]):
        if n2D[num1,num2] < np.mean(n2D)/2 or n2D[num1,num2] > np.mean(n2D)*2:
            n2D[num1,num2] = np.mean(n2D)
plt.pcolor(n2D, cmap = 'inferno')
plt.title(filebase + ' n Plot')
for num in range(0,H2D.shape[1]):
    if num in [0,20,40,60,80,100]:
        my_xticks = np.append(my_xticks,round(float(num*(xCoord.max()-
xCoord.min())/H2D.shape[1]),2))
    else:
        my_xticks = np.append(my_xticks,"")
plt.xticks(range(0, H2D.shape[1]), my_xticks)
my_yticks = []
for num in range(0,H2D.shape[0]):
    if num in [0,5,10,15,20,25,30,35,40,45,50,55,60,65,70,75,80,85,90,95,100]:
        my_yticks = np.append(my_yticks,round(float(num*(yCoord.max()-
yCoord.min())/H2D.shape[0]),2))
    else:
        my_yticks = np.append(my_yticks,"")
plt.yticks(range(0, H2D.shape[0]), my_yticks)
plt.colorbar()
plt.savefig(fileDirectory + filebase + '_nPlot.jpg')

plt.clf()
YSIndentAverage = np.mean(YSSave, axis=1)

```

```

YS2D = YSIndentAverage.reshape((xDim, yDim))
for num1 in range(YS2D.shape[0]):
    for num2 in range(YS2D.shape[1]):
        if YS2D[num1,num2] < np.mean(YS2D)/2 or YS2D[num1,num2] > np.mean(YS2D)*2:
            YS2D[num1,num2] = np.mean(YS2D)
plt.pcolor(YS2D, cmap = 'inferno')
plt.title(filebase + ' YS Plot')
for num in range(0,H2D.shape[1]):
    if num in [0,20,40,60,80,100]:
        my_xticks = np.append(my_xticks,round(float(num*(xCoord.max()-
xCoord.min())/H2D.shape[1]),2))
    else:
        my_xticks = np.append(my_xticks,"")
plt.xticks(range(0, H2D.shape[1]), my_xticks)
my_yticks = []
for num in range(0,H2D.shape[0]):
    if num in [0,5,10,15,20,25,30,35,40,45,50,55,60,65,70,75,80,85,90,95,100]:
        my_yticks = np.append(my_yticks,round(float(num*(yCoord.max()-
yCoord.min())/H2D.shape[0]),2))
    else:
        my_yticks = np.append(my_yticks,"")
plt.yticks(range(0, H2D.shape[0]), my_yticks)
plt.colorbar()
plt.savefig(fileDirectory + filebase + '_YSPlot.jpg')

plt.clf()
EIndentAverage = np.mean(ESave, axis=1)
E2D = EIndentAverage.reshape((xDim, yDim))
for num1 in range(E2D.shape[0]):
    for num2 in range(E2D.shape[1]):
        if E2D[num1,num2] < np.mean(E2D)/2 or E2D[num1,num2] > np.mean(E2D)*2:
            E2D[num1,num2] = np.mean(E2D)

```

```

plt.pcolor(E2D, cmap = 'inferno')
plt.title(filebase + ' E Plot')
for num in range(0,H2D.shape[1]):
    if num in [0,20,40,60,80,100]:
        my_xticks = np.append(my_xticks,round(float(num*(xCoord.max()-
xCoord.min())/H2D.shape[1]),2))
    else:
        my_xticks = np.append(my_xticks,"")
plt.xticks(range(0, H2D.shape[1]), my_xticks)
my_yticks = []
for num in range(0,H2D.shape[0]):
    if num in [0,5,10,15,20,25,30,35,40,45,50,55,60,65,70,75,80,85,90,95,100]:
        my_yticks = np.append(my_yticks,round(float(num*(yCoord.max()-
yCoord.min())/H2D.shape[0]),2))
    else:
        my_yticks = np.append(my_yticks,"")
plt.yticks(range(0, H2D.shape[0]), my_yticks)
plt.colorbar()
plt.savefig(fileDirectory + filebase + '_EPlot.jpg')

```

```

#WORKING MAKING 3D PLOTS

```

```

#

```

```

#

```

```

#from mpl_toolkits.mplot3d import Axes3D

```

```

#import matplotlib.pyplot as plt

```

```

#from matplotlib import cm

```

```

#from matplotlib.ticker import LinearLocator, FormatStrFormatter

```

```

#import numpy as np

```

```

#

```

```

#

```

```

#fig = plt.figure()

```

```
#ax = fig.gca(projection='3d')
#
#plt.clf()
#X = np.linspace(xCoord.min(),xCoord.max(),xCoord2D.shape[1]-1)
#Y = np.linspace(yCoord.min(),yCoord.max(),yCoord2D.shape[0]-1)
#X, Y = np.meshgrid(X, Y)
#Z = H2D
#surf = ax.plot_surface(X, Y, Z, cmap=cm.coolwarm,linewidth=0, antialiased=False)
#fig.colorbar(surf, shrink=0.5, aspect=5)
#plt.show()
```